THESIS

LINEAR COMBINATIONS OF GNSS PHASE OBSERVABLES TO IMPROVE AND ASSESS TEC ESTIMATION PRECISION

Submitted by

Brian W. Breitsch

Department of Electrical and Computer Engineering

In partial fulfillment of the requirements

For the Degree of Master of Science

Colorado State University

Fort Collins, Colorado

Fall 2017

Master's Committee:

Advisor: Jade (Yu) Morton

Charles Rino
Anton Betten

ABSTRACT

LINEAR COMBINATIONS OF GNSS PHASE OBSERVABLES TO IMPROVE AND ASSESS TEC ESTIMATION PRECISION

One of the principal observations derived from GNSS (Global Navigation Satellite Systems) signals is ionospheric total electron content (TEC), which is a measure of the density of free electrons (i.e. ionosphere plasma density) integrated along the signal path. TEC is typically computed using the difference of dual-frequency signals from a GNSS satellite, thereby taking advantage of the frequency dispersive effects of ionosphere plasma on microwave-band propagation. However, it is difficult to distinguish between the ionosphere and other frequency-dependent effects, such as multipath and satellite antenna phase effects. Newly available triple-frequency GNSS signals allow computation of geometry-ionosphere-free combinations (GIFC) that specifically highlight the impact of residual errors from these effects. This work aims to: 1) introduce a framework for choosing linear estimator coefficients for GNSS parameters, 2) use this system to derive triple-frequency TEC estimator and GIFC coefficients, 3) introduce and summarize typical GIFC signals from real triple-frequency GPS data, 4) highlight the various frequency-dispersive effects that pervade these signals, and 5) use statistics from GIFC signals to assess the impact of error residuals on TEC estimates made using GPS signals.

ACKNOWLEDGEMENTS

This work would not have been possible without all the feedback and support of many people with whom I have shared and discussed this work. I sincerely thank you all. First and foremost I would like to thank my advisor Dr. Jade Morton for her mentorship and guidance. Throughout the development of this work, she has paired her high expectations with genuine compassion and empathy. Working with her has been a rewarding experience. I would also like to thank my committee members Dr. Charles Rino and Dr. Anton Betten for their valuable comments and feedback.

I have received valuable comments and technical assistance from my peers, co-workers, and CSU staff. I would like to especially thank Jack, Harrison, and Ian for their comments and feedback on my work, Steve and Greg for their assistance with data and other technical matters, and Katya for her guidance with procedure and paperwork.

I would like to give special thanks to Kira for her rigorous proofreading and grammatical corrections. Also, thank you to my brothers, who have provided encouragement and valuable perspectives from outside my field. Finally, thank you to my parents for their unending love, patience, and support.

This project was supported by:

- AFRL contract #FA8650-14-1735
- NASA grant #NNX15AT54G
- a grant from AOARD to Nanyang Technological University

TABLE OF CONTENTS

LIST OF TABLES

LIST OF FIGURES

CHAPTER 1: BACKGROUND AND MOTIVATION

Ionosphere Total Electron Content (TEC) is an important measurement used to study and characterize Earth's ionosphere and the phenomena that affect it. Multi-frequency transmissions from Global Navigation Satellite Systems (GNSS) can be used to measure TEC by taking advantage of the ionosphere's frequency-dispersive effect on microwave-band electromagnetic wave propagation. While traditional GNSS-based TEC estimation uses signals at two different frequencies, many modern GNSS now transmit signals at three frequencies (and future GNSS may transmit many more frequencies). These new signals provide better information on propagation and instrumentation effects present in GNSS observables, including that of ionosphere TEC.

This work focuses on multi-frequency GNSS estimates of TEC and using triple-frequency GPS observations to consider the precision of such estimations. In this first chapter, we briefly discuss Earth's ionosphere and GNSS as they relate to TEC estimation. In the second chapter, we introduce an underlying physical model and relate it to phase measurements made by GNSS receivers. Then we introduce a general method for choosing model estimators that are linear combinations of these phase measurements and consider application of this method to triple-frequency signals from Global Positioning System (GPS) satellites. Using this method, we derive the geometry-ionosphere-free combination (GIFC) of GNSS observables, which is an indicator of residual systematic and stochastic errors present in GNSS observables. In the third chapter, we use real GPS data to examine the GIFC and consider the systematic errors it exposes. We present a qualitative and statistical assessment of the GIFC from triple-frequency GPS signals. Lastly, we use GIFC statistics to characterize the precision of multi-frequency TEC estimates. In chapter four, we briefly discuss the implications of the results and consider routes for future work.

1.1 Earth's Ionosphere

The ionosphere is a volume of atmosphere surrounding Earth between roughly 60-1000 km altitude. Various ionization sources cause plasma to form in this region, with the primary among these being photo-ionization from the Sun. Secondary ionizing agents include energetic particle precipitation, meteorites, and lightning. The spatial-temporal distribution of this plasma is impacted by many factors such as the day-night cycle, solar cycle, geomagnetic fields, neutral atmospheric winds, space weather events, etc [1].

1.1.1 Radio Propagation in the Ionosphere

The ionosphere is well-known for its frequency-dependent effects on radio wave propagation. These effects were first demonstrated by Guglielmo Marconi at the premier of trans-Atlantic radio transmission in 1901 [2]. Since then, radio signals have been used as a tool to study the ionosphere, while the ionosphere has been used as a tool to aid in global radio communication. Radiosonde, coherent radar, incoherent scatter radar, and GNSS receivers are all radio instruments commonly used to measure the ionosphere.

In terms of its effect on microwave-band electromagnetic waves, the ionosphere can be considered a cold, magnetized, collisionless plasma. This means that its refractive index is described by the collisionless form of the Appleton-Hartree equation:

$$n^2 = 1 - \frac{X}{1 - \frac{\frac{1}{2}Y^2\sin^2\theta_B}{1-X} \pm \frac{1}{1-X}\left(\frac{1}{4}Y^4\sin^4\theta_B + Y^2\cos^2\theta_B(1-X)^2\right)^{\frac{1}{2}}} \tag{1.1}$$

$$X = \frac{\omega_p^2}{\omega^2} \qquad\qquad Y = \frac{\omega_H}{\omega}$$

where ω is the wave angular frequency, ω_p is the electron plasma frequency, ω_H is the electron gyro frequency, θ_B is the angle between the wave vector and the ambient magnetic field, and the $\pm$ is dependent upon wave polarization and orientation relative to the magnetic field.

The omega terms can be further decomposed as:

$$\omega = 2\pi f \tag{1.2}$$

$$\omega_p = \sqrt{\frac{N_e e^2}{\epsilon_0 m}} \tag{1.3}$$

$$\omega_H = \sqrt{\frac{B_0|e|}{m}} \tag{1.4}$$

where f is the wave frequency, N_e is the plasma density (or, equivalently, the free-electron density), ϵ_0 is the permittivity of free space, e is the electron charge, m is the rest mass of an electron, and B_0 is the ambient magnetic field strength.

The expression in Equation 1.1 does not lend itself to direct application. Instead it is simplified using a Taylor's series expansion in $\frac{1}{f}$ for f near the frequency of propagation. For L-band frequencies, X and Y are much less than 1. After dropping insignificant terms for frequencies relevant to this work, the expression becomes:

$$n = 1 - \frac{1}{2}X \pm \frac{X|Y\cos\theta_B|}{2} - \frac{1}{8}X^2 \pm \mathcal{O}(\frac{1}{f^5}) \tag{1.5}$$

The first-order term $-\frac{1}{2}X$ is proportional to $\frac{1}{f^2}$ and accounts for most of the ionosphere range error. Second and higher-order terms are on the order of a couple centimeters or less [3]. As is the case for plasmas, the magnitude of the refractive index n is always less than unity. As a result, there is a perceived phase advance for microwave-band signals that traverse the ionosphere.

1.1.2 Ionosphere Range Error and Total Electron Content

The ionosphere range error for an electromagnetic wave propagating through it is defined to be the integrated effect of the ionosphere refractive index minus the signal path length. Considering only the first-order ionosphere effect, its expression is:

$$I = \int_{\text{rx}}^{\text{tx}} (n-1)\ ds \approx \int_{\text{rx}}^{\text{tx}} -\frac{1}{2}X\ ds \tag{1.6}$$

Here, rx and tx denote the endpoints of signal propagation and s is the signal path. Using

expressions 1.2 and 1.3 to expand X, this becomes:

$$I = -\frac{\kappa}{f^2} \int_{\text{rx}}^{\text{tx}} N_e \, ds \tag{1.7}$$

where $\kappa = \frac{e^2}{8\pi^2 \epsilon_0 m_e} \approx 40.3$.

Total electron content (TEC) is defined to be the integrated quantity of the free-electron density (i.e. plasma density) N_e along some path. The expression for the first-order ionosphere effect in Equation 1.7 contains the expression for TEC, which is:

$$\text{TEC} = \int_{\text{rx}}^{\text{tx}} N_e \, ds \tag{1.8}$$

It is usually convenient to express TEC in TEC units, where $1\text{TECu} = 1 \times 10^{16} \frac{\text{electrons}}{m^2}$. As such, we define $\kappa_u = \kappa \times 10^{16}$ and express I as:

$$I = -\frac{\kappa_u}{f^2} \text{TECu} \tag{1.9}$$

1.1.3 Geomagnetic Field

Expressions for the phase refractive index in equations 1.1 and 1.5 reveal that an important aspect of the ionosphere is that it lies within influence of Earth's magnetic field. The so-called geomagnetic field is a magnetic dipole with field lines leaving near the geographic South pole and entering near the geographic North pole. The orientation of a radio wave vector relative to these field lines plays a role in determining higher-order terms for ionosphere propagation error. This field is also important because it constrains the movement of ionosphere plasma. The charged plasma particles move more freely parallel to the magnetic field, so density structures in the plasma tend to spread out along field lines [1].

1.1.4 Plasma Density Features

The various factors that influence the ionosphere will cause structures to form in the plasma density. Examples of structures that can normally be seen in ionosphere plasma density are the E and F region peaks, daytime ionization enhancements, and the equatorial

ionization crests. The terms D, E, or F layer describe concentrations of plasma that commonly occur at specific heights. Figure 1.2 shows a nominal vertical plasma density profile, revealing typical daytime structure of the E and F layers at low latitudes. Vertical TEC (vTEC), defined as TEC measured in the zenith direction for a given latitude and longitude, is often used to study large-scale features. Figure 1.3 shows a nominal global distribution of vTEC that reveals the equatorial ionization crests.

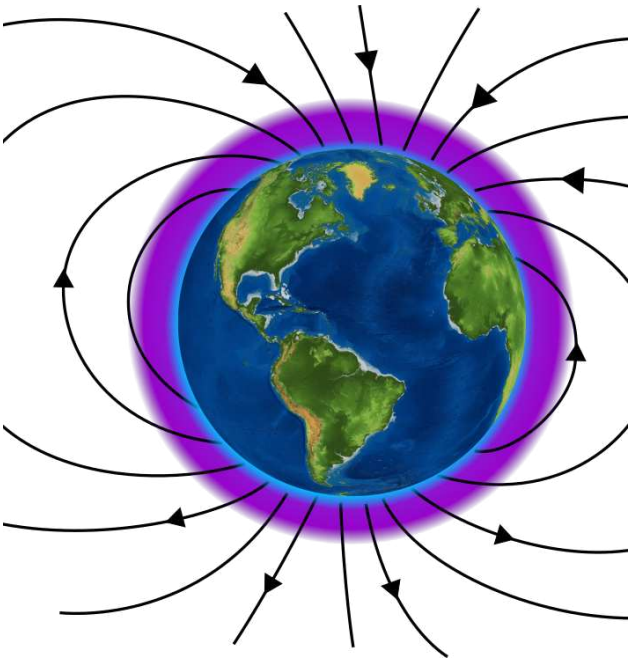

Figure 1.1: Depicts how the ionosphere is embedded in Earth's geomagnetic field. Note how field lines leave Earth from the geographic South pole and enter through the geographic North pole. The magnetic inclination, which is the angle between the magnetic field vector and the tangent to Earth's surface, changes continuously over latitude with values of $\pm 90^\circ$ at the geomagnetic South/North poles and 0° at the geomagnetic equator.

The various factors that influence the ionosphere can cause disturbances that manifest as plasma enhancements and depletions. Incoherent scatter radar measurements are often used to scan the plasma structure at medium and large scales [6]. Networks of GNSS receivers are used to map vTEC variations in order to monitor traveling ionosphere disturbances (TIDs) [7]. These disturbances are known to arise from terrestrial activities such as earthquakes, volcanic eruptions, and tsunamis, making the ionosphere an important tool for studying

these phenomena [8]. At high latitudes, energetic particle precipitation causes polar cap patches and auroral-specific structures. The effects of solar storms can be seen in plasma structures at all latitudes. The most robust observations of these medium to large-scale plasma structures combine radars and GNSS using data assimilation models.

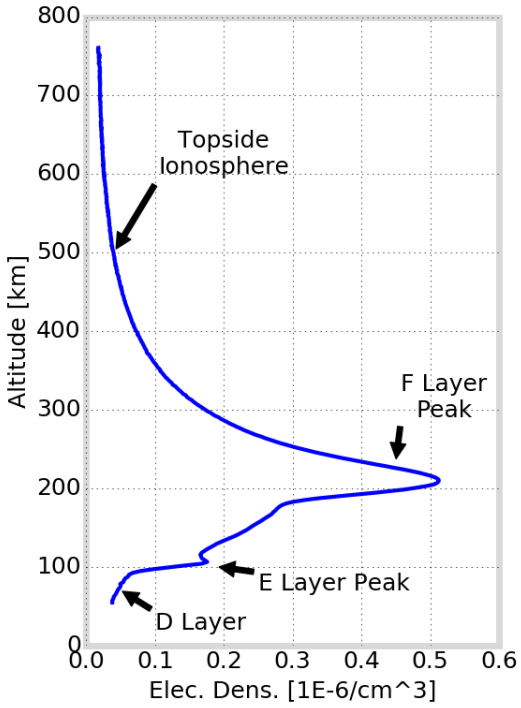

Figure 1.2: Shows typical daytime vertical profiles of plasma density. The profile has a mean geographic latitude of $\approx 18^\circ$ N. Large-scale vertical structure in the ionosphere is typically classified as one of D region, E region, F region, or topside ionosphere, all of which the figure annotates. This profile was generated by the COSMIC Data Analysis and Archive Center (CDAAC) using GPS radio occultation measurements from the FORMOSAT-1 satellite [4].

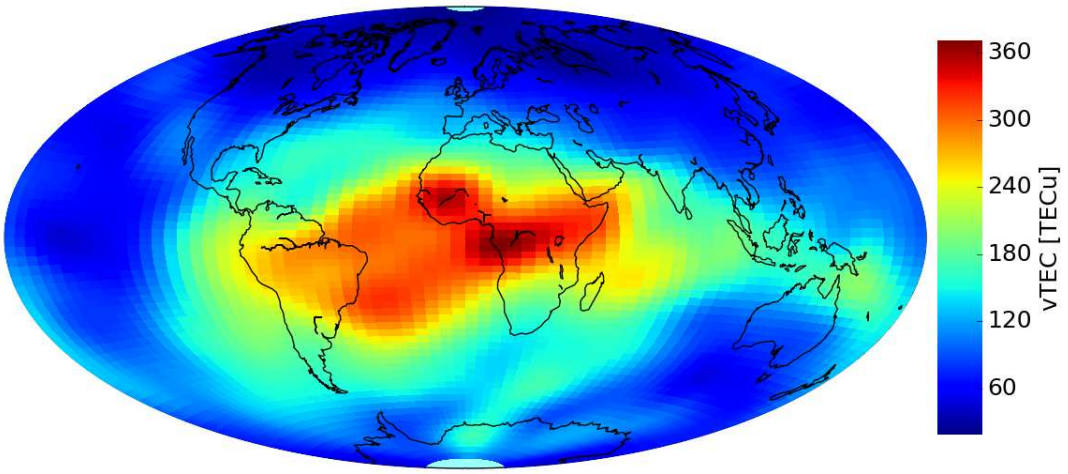

Figure 1.3: Shows a nominal global distribution of TEC measured in the zenith (vertical) direction. Higher TEC values indicate more plasma in that region. The map epoch 14:00 UTC is the local time for the central (prime) meridian. As it is only a few hours after daytime noon, this region experiences large vTEC values. This map was generated by the International GNSS Service (IGS) using their global network of GNSS receivers [5].

1.2 GNSS

Global Navigation Satellite Systems (GNSS) consist of satellite constellations and ground infrastructure that provide ranging signals whose primary use is for accurate position and timing estimation by users around the world. These systems transmit signals in the L-band (1-2 GHz), which is high enough to penetrate the ionosphere but low enough to avoid too much signal attenuation during their long journey from satellite to ground. This makes GNSS signals sensitive – and therefore vulnerable – to structures and irregularities in the ionosphere plasma.

Most GNSS satellites transmit multiple signals at various frequencies in order to aid in the estimation of ionosphere effects and to provide redundancy in order to improve reliability. These signals are comprised of sinusoidal carriers modulated by ranging codes. In principle, GNSS receivers measure phase and amplitude of the carrier and phase of the ranging code. Carrier and code phases are often expressed as pseudoranges (i.e. in units of length) in order to reflect the physical range between receiver and satellite for which they are purposed to measure. The ionosphere range error I is a significant term in pseudorange expressions. Equation 1.10 describes a carrier phase pseudorange measurement model for a single GNSS satellite:

$$\Phi_i = r + c\Delta t + T + I_i + \lambda_i N_i + H_i + S_i + \epsilon_i \tag{1.10}$$

Here, subscripts i denote quantities pertaining to a given signal whose carrier frequency is f_i. Terms without subscripts are the same for all signals from a particular satellite. The quantities themselves are described as follows:

- r - range between satellite and receiver antenna phase centers
- $c\Delta t$ - range error due to relative offset Δt between satellite and receiver clocks, where c is the speed of light
- T - neutral atmosphere range error

- I - ionosphere range error (from equations 1.6 or 1.7)
- λN - range error due to carrier phase ambiguity, which is an unknown integer cycle offset N multiplied by carrier wavelength λ
- H - satellite and receiver hardware delays
- S - unmodeled systematic effects; multipath, higher-order ionosphere terms, etc.
- ϵ - all stochastic effects, such as thermal noise

Figure 1.4 shows a GNSS satellite as it relates to Earth and the ionosphere. The ionospheric volume accounts for between 1-5% of the propagation distance while Earth's neutral atmosphere, which is significant between roughly 0 - 60 km, accounts for less than .05 % of the propagation distance. The rest of the GNSS propagation path can be considered in a vacuum. Table 1.1 describes nominal ranges for the quantities in the carrier pseudorange model.

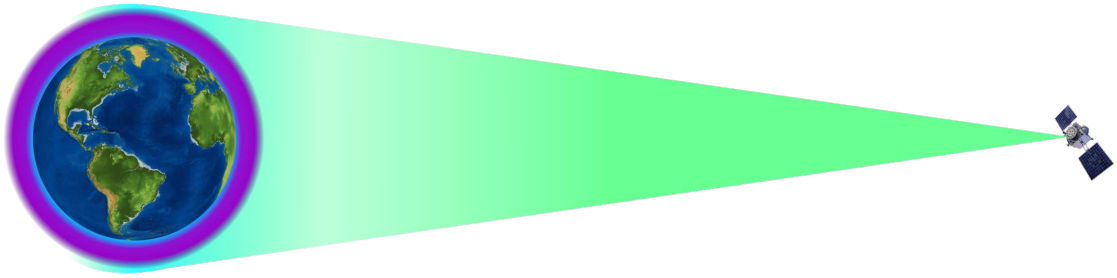

Figure 1.4: Depicts typical Earth-ionosphere-satellite geometry for GNSS constellations. Most satellites have transmission patterns that provide hemispheric signal coverage.

1.2.1 GPS

The Global Positioning System (GPS) is a GNSS controlled and maintained by the United States of America. The GPS constellation first became operational in the 1980s with the launch of eleven Block I satellites. Since then, the GPS satellite has gone through several

iterations. As of 2017, the last of the second-generation GPS satellites has been launched, and a third-generation constellation is in preparation.

Table 1.1: Nominal ranges for GNSS carrier pseudorange observation model parameters [9].

Parameter	Description of Parameter Size
r	20,000 - 26,000 km
$c\Delta t$	receiver-dependent
T	2.5-25 m for receiver on ground
I	1-150 m for receiver on ground
λN	receiver-dependent; large, unknown, constant bias
H	$\pm$ 25 m for satellite and receiver hardware biases [10]
S	see Section 1.2.5
ϵ	receiver-dependent; less than 4 mm for high-quality receiver

The full active GPS constellation consists of 32 satellites in six orbital planes. Their orbits are approximately circular with radii of around 26,000 km. The corresponding orbital periods are approximately one-half mean sidereal day, which is equal to 11 hours, 58 minutes, 2.05 seconds. The period is such that a given location on Earth's surface will see a particular GPS satellite at least once every 24 hours, with the satellite's pass occurring approximately 4 minutes sooner each day.

The last set of second-generation GPS satellites is Block IIF (for "Block 2 Follow-on"). This set of 12 satellites are of particular interest because they each transmit three signals at distinct frequencies. These signals are called L1CA, L2C, and L5 (which we hereafter refer to as L1, L2, and L5) and their carrier frequencies are given in Table 1.2. Figure 1.5 shows the when each triple-frequency satellite started transmitting. Four satellites (G01, G24, G25, G27) are highlighted in blue; these are the satellites that will be the focus of our analysis in Chapter 3.

Table 1.2: Carrier frequencies corresponding to each GPS signal.

Signal	Carrier Frequency [GHz]
L1CA	1.57542
L2C	1.22760
L5	1.17645

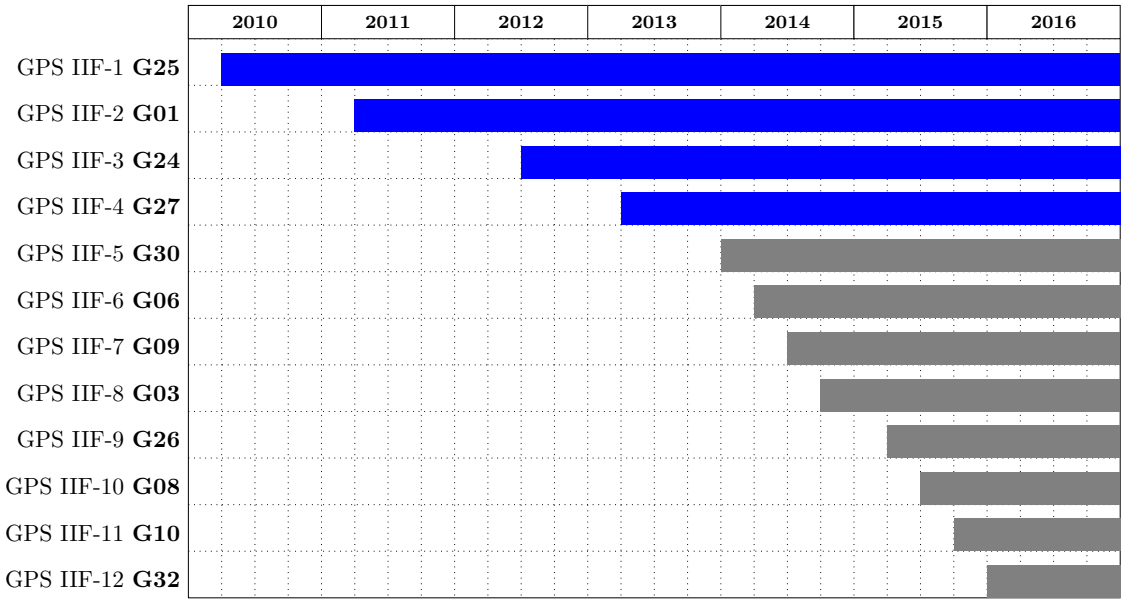

Figure 1.5: Shows period of signal availability for GPS Block IIF satellites. Satellite names followed by universal identifiers (in bold) are shown on the left. Blue bars are used to indicate satellite whose data we use in this work. Each has been transmitting triple-frequency GPS signals since 2013.

1.2.2 TEC Estimation Using GNSS

Phase measurements of multi-frequency signals from a GNSS satellite can be used to estimate TEC. Using the model in Equation 1.10, consider the difference between two carrier phase pseudorange measurements Φ_1 and Φ_2 for carriers at two distinct frequencies f_1 and f_2, while treating systematic and stochastic errors as negligible. The expression for their difference is given by:

$$\begin{aligned} \Phi_1 - \Phi_2 &= (I_1 - I_2) + (\lambda_1 N_1 - \lambda_2 N_2) + (H_1 - H_2) \\ &\approx -\kappa_u \left(\frac{1}{f_1^2} - \frac{1}{f_2^2} \right) \mathrm{TECu} + (\lambda_1 N_1 - \lambda_2 N_2) + \Delta H_{1,2} \end{aligned} \tag{1.11}$$

Here, we assume only first-order ionosphere effects and use the expression for I from Equation 1.9. The term $\Delta H_{1,2} = H_1 - H_2$ contains the so-called inter-frequency hardware biases of both satellite and receiver.

It is apparent from Equation 1.11 that if ambiguity and hardware bias terms can be eliminated then TEC can be estimated as:

$$\text{TECu} = \frac{\Phi_2 - \Phi_1}{\kappa_u \left(\frac{1}{f_1^2} - \frac{1}{f_2^2} \right)} \tag{1.12}$$

This is the traditional dual-frequency estimation of TEC. GPS signals L1 and L2 are commonly used to estimate TEC in this way.

1.2.3 Carrier Ambiguity and Hardware Bias Resolution in GNSS

There are many techniques to address the ambiguity and bias terms in pseudorange phase differences. These techniques are often the focus of work on TEC estimation. The carrier ambiguity terms can be solved using measurement-domain techniques, such as code-carrier leveling, or using integer-least-squares techniques, such as LAMBDA [11]. Inter-frequency hardware biases (IFBs), which are stable constants for a given satellite or given receiver, must be estimated by applying some sort of ionosphere model or constraint. Methods such as the one in [10] use a priori models of the ionosphere. Others, such as in [12] or [13], use networks of receivers to estimate an ionosphere model in real time. [14] discusses an algorithm that uses a simple, linear-gradient ionosphere model and a single receiver to calibrate receiver IFB.

Multi-frequency adaptations of ambiguity resolution and IFB determination techniques have also been explored. [15], [16], and [17] discuss ambiguity resolution in the context of triple-frequency GNSS. [18] characterizes the different IFBs for triple-frequency GPS satellites and signals. [19] applies approaches from both domains, using a code-carrier leveling technique along with a least-squares estimation of TEC and relative IFBs in the context of triple-frequency GNSS.

1.2.4 Examples of GPS TEC Estimations

Here, we present examples of dual-frequency TEC estimations using triple-frequency GPS signals. We do this in order to demonstrate the presence of systematic errors that corrupt

TEC estimates and thereby motivate the work laid out in this thesis. Using a method similar to that in [19], we solve for carrier ambiguities and relative receiver IFBs. We then use the method in [14] to estimate absolute receiver IFBs. Using these carrier ambiguities and IFBs to correct our carrier pseudorange measurements, we can estimate TEC using Equation 1.12 for the appropriate frequencies. Details on the exact method implementation are given in Appendix AA. Figure 1.6 shows examples of these TEC estimates using GPS L1/L2 and L1/L5 signal combinations. Although their overall shapes match, a varying discrepancy exists between the two estimates. We attribute this discrepancy to the systematic error terms S from Equation 1.10.

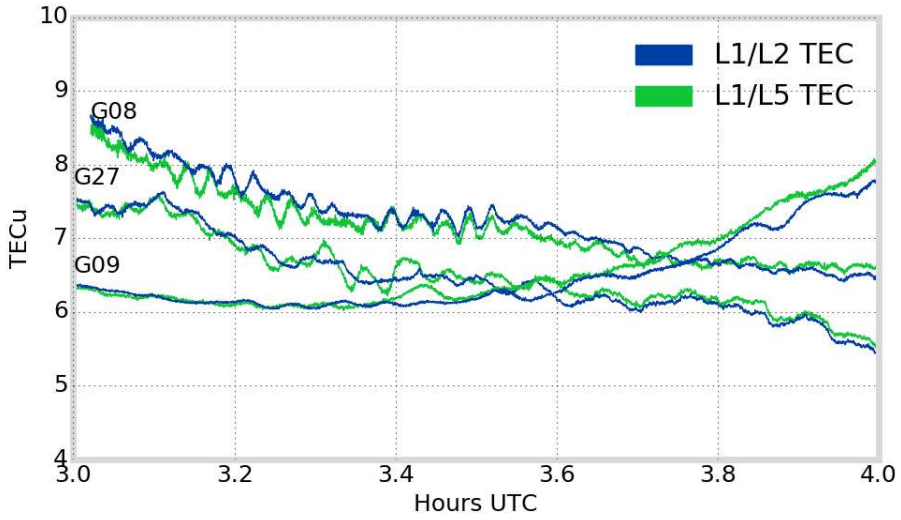

Figure 1.6: Dual-frequency estimates of TEC using GPS L1/L2 and L1/L5 signal combinations. Estimates for satellites G06, G09, and G27 are shown for a receiver in Poker Flat, Alaska on 2016-01-02. Varying discrepancies between the two estimates indicate the presence of systematic errors.

1.2.5 Summary of Known Systematic Errors

Having observed the effect of systematic errors in dual-frequency TEC estimation, the question arises: what are the systematic effects that cause this discrepancy, and how can we mitigate these effects to achieve optimal TEC estimation precision? The TEC discrepancy

shows oscillatory patterns towards both ends of the pass where the satellite is at low elevation. This behavior is indicative of multipath, which refers to the error caused by multiple signal reflections combining with and distorting the direct signal at the receiver. The carrier phase multipath effect is dependent upon the antenna environment, e.g. the orientation and reflectiveness of surrounding surfaces. Multipath simulations in [20] show GPS L1/L2 carrier differences reaching up to ± 4 cm.

Other ionospheric effects may also play a role, though their effect should not show the oscillatory behavior of multipath. In general, residual error from the higher-order ionosphere terms for GPS L1/L2 difference ranges from -2 to 2.5 cm. Excess path length due to ionosphere refraction effects can also be significant, reaching values of 3 cm or higher in the GPS L1/L2 difference for low-elevation satellites ($< 5^\circ$) [21].

A third plausible culprit is satellite and receiver antenna phase effects. GNSS satellite antenna phase center variations are modeled by the International GNSS Service (IGS) for application to precise point positioning [5]. However, their most recent products still only provide mean phase center variations for the GPS L1/L2 ionosphere-free combination [22]. Work from [23] attempts to characterize the antenna phase center and variations for the GPS Block IIF-1 satellite. They determined that a full analysis on the phase center variations involving the L5 signal will be feasible once a sufficient global constellation transmitting triple-frequency signals is achieved. Another effect related to satellite antenna phase is antenna phase windup, which occurs due to rotation of the satellite antenna over the duration of its pass. This results in extra accumulated phase at the receiver, which, for given carrier pseudorange measurement, can be up to several centimeters [24].

1.3 Motivation for This Work

In this work, we present linear estimators – that is, linear combinations of the GNSS phase pseudorange observables – for TEC and related model parameters. Linear combinations of GNSS observables have been widely studied. The coming of next-generation of GNSS and

triple-frequency signals prompted investigation into optimal triple-frequency combinations for various applications, including cycle slip estimation, ambiguity resolution, ionosphere-free combinations, and TEC estimation, some of which we discussed in Section 1.2.3. Much of the work surrounding the application of multi-frequency GNSS linear combinations aims to improve ambiguity resolution and IFB estimation. While these objectives are crucial for accurate retrieval of TEC, they will not be considered in this work. Instead, we choose to ignore all terms considered as biases in our signal model and to focus on the precision, rather than overall accuracy, of TEC estimations.

The work most closely related to that which we present here can be found in [25] and [26]. The first author introduces optimal coefficients for ionosphere-free, range-preserving linear combinations in the context of triple-frequency GPS. These coefficients are essentially estimators of the non-dispersive terms from Equation 1.10 that remove the ionosphere component. Their results match those that we present in Section 2.5. The second author discusses using triple-frequency GNSS measurements specifically in the context of TEC estimation. The first part of their work discusses ambiguity and IFB estimation. In the second part, a linear system relating TEC and relative carrier ambiguities to the observed carrier pseudorange differences between L1/L2 and L1/L5 signals is solved. It can be shown that, if carrier ambiguities are properly resolved, then the TEC estimate from this method should match the triple-frequency TEC estimate we present in Section 2.4.

One of the main contributions of this work is a general framework, rooted in the fundamentals of linear inverse theory, for choosing coefficients for linear estimators of GNSS model parameters. We derive optimal multi-frequency estimator coefficients for the geometry (non-dispersive) term and for TEC based on this framework, and provide their closed-form solutions for the case of triple-frequency GNSS. While the triple-frequency geometry-estimator coefficients are presented in [25], this is, to the best of our knowledge, the first publication containing the triple-frequency TEC estimator coefficients. Furthermore, we present a third set of coefficients for the geometry-ionosphere-free combination (GIFC), which provides

information on the systematic errors that pervade GNSS measurements and corrupt TEC estimates. The main results of our work are characterization of the GIFC and relation of its statistical deviation to precision bounds for TEC estimates.

The motivation for the characterization of the GIFC and precision bounds for TEC estimates stems from real-world scientific and engineering applications, which demand increasing precision in TEC and other parameter estimates. In [27] it is reported that the effect of a medium-scale TID on GNSS measurements is on the order of tenths of one TEC unit. At the same time, this level of precision is needed for centimeter-level positioning solutions. Understanding the precision of TEC estimates and the nature of the systematic errors that affect them is paramount to pushing the boundaries of these types of applications.

We qualify here that the characterization of TEC estimation errors observed using the GIFC does not provide a complete assessment of errors impacting TEC estimation. As we show in Section 2.7, there is a component of TEC error residuals that is "TEC-like" and therefore unobservable. We make certain assumptions in an attempt to describe the overall error, but it is possible that other effects, such as diffraction by ionosphere irregularities, can dominate this component of TEC errors.

CHAPTER 2: LINEAR ESTIMATION OF GNSS PARAMETERS

In this chapter, we discuss linear estimation of GNSS model parameters from carrier phase pseudorange observables. We choose these model parameters to reflect the quantities in Equation 1.10. By introducing the general linear estimation problem, we will be able to unify conventional TEC estimation with optimal linear estimation methods involving multi-frequency GNSS signals.

2.1 Simplified Model of GNSS Phase Observable

Before we introduce the estimation problem, we make the following simplifications. First, we consider observations only from one satellite transmitting two or more signals at different frequencies. We also group all non-dispersive terms from Equation 1.10 (i.e. terms independent of signal frequency, such as r, $c\Delta t$, and T) into one quantity G, called the geometric term. Since this work is concerned with the precision rather than accuracy of our observables and corresponding TEC estimates, we ignore ambiguity N and bias terms H altogether. We also assume that ϵ_i are zero-mean and normally-distributed. Applying these assumptions to Equation 1.10, we obtain the following model for carrier pseudorange measurements:

$$\Phi_i = G + I_i + S_i + \epsilon_i \tag{2.1}$$

Let us make an additional simplification to our model by assuming that I_i represents only the first-order ionosphere effect, while letting S_i absorb the other ionospheric terms. This allows us to express the ionospheric terms I_i as proportional to TECu, as in Equation 1.9.

2.2 Linear Observation Model and Inverse Problem

Consider Φ_i for m signals of distinct frequencies from a particular GNSS satellite. Let our model parameters be G, TECu, and the terms S_i corresponding to each signal. Equation 2.1 describes a linear model for each Φ_i in terms of our model parameters, and the linear system can be expressed as:

$$\mathbf{\Phi} = \mathbf{A}\mathbf{m} + \epsilon \tag{2.2}$$

where $\mathbf{\Phi} = [\Phi_1, \cdots, \Phi_m]^T$, $\epsilon = [\epsilon_1, \cdots, \epsilon_m]^T$, $\mathbf{m} = [G, \text{TECu}, S_1, \cdots, S_m]^T$, and

$$\mathbf{A} = \begin{bmatrix} 1 & -\frac{\kappa_u}{f_1^2} & 1 & 0 & \cdots & 0 \\ 1 & -\frac{\kappa_u}{f_2^2} & 0 & 1 & \cdots & 0 \\ \vdots & & & & \ddots & \\ 1 & -\frac{\kappa_u}{f_m^2} & 0 & \cdots & & 1 \end{bmatrix} \tag{2.3}$$

Note that $\mathbf{\Phi}, \epsilon \in \mathbb{R}^m$ and $\mathbf{m} \in \mathbb{R}^{m+2}$ so that $\mathbf{A} \in \mathbb{R}^{m \times m+2}$.

Solutions to this linear inverse problem provide a set of coefficients for estimating model parameters $\mathbf{m}$ in terms of $\mathbf{\Phi}$. That is

$$\hat{\mathbf{m}} = \mathbf{A}^* \mathbf{\Phi} \tag{2.4}$$

where $\mathbf{A}^* \in \mathbb{R}^{m+2 \times m}$ is the model estimator. One solution is the left pseudo-inverse $\mathbf{A}^T \left(\mathbf{A}\mathbf{A}^T\right)^{-1}$. However, this produces a poor model estimate since it treats each parameter with equal weight. To create a good model estimator, we must apply a priori knowledge about G, I_i, and Φ_i. Considering the nominal parameter ranges in Table 1.1, it is reasonable to make the following coarse assumption:

$$|G| \gg |I_i| \gg |S_i| \tag{2.5}$$

We could apply this knowledge to obtain more suitable estimator $\mathbf{A}^*$ for the whole model $\mathbf{m}$. Instead, we choose the longer and more insightful route of establishing linear estimators for each model parameter separately. This allows us to consider our estimates of G and TECu as they relate to conventional methods for extracting these terms. Estimates of

individual model parameters are just linear combinations of the phase observables Φ_i, which we introduce in the next section.

2.3 Linear Combinations of GNSS Observables

Our goal in constructing linear combinations of Φ_i is to estimate individual model parameters, that is, to construct rows of $\mathbf{A}^*$. Given m phase pseudorange observables $\Phi_1, \cdots, \Phi_m$, we can construct a linear combination using coefficients $c_1, \cdots, c_m$ as:

$$\Phi^* = \sum_i c_i \Phi_i = \langle \mathbf{C} | \mathbf{\Phi} \rangle \tag{2.6}$$

where $\mathbf{C} = [c_1, \cdots, c_m]^T$ is the coefficient vector.

If we can bound systematic errors for each Φ_i as $|S_i| \leq |S_i|_{\max}$ then we can bound systematic error term in the resultant linear combination as:

$$|S^*| \leq \sum_i |c_i| |S_i|_{\max} \tag{2.7}$$

For stochastic errors, the law of error propagation gives the stochastic error variance of the linear combination as:

$$\sigma^2_{\epsilon^*} = \mathbf{C}^T \mathbf{\Sigma}_\epsilon \mathbf{C} \tag{2.8}$$

where $\mathbf{\Sigma}_\epsilon$ is the covariance matrix of stochastic noise terms ϵ_i. The expressions for linear combination systematic error bound and stochastic error variance are useful for defining objectives when choosing optimal linear combination coefficients.

2.3.1 Linear Combination Coefficient Constraints

Keeping in mind that we wish to estimate model parameters G, TECu and S_i, we introduce the following useful coefficient constraints.

$$\sum_i c_i = 0 \qquad \text{(geometry-free constraint)} \tag{2.9}$$

$$\sum_i \frac{c_i}{f_i^2} = 0 \qquad \text{(ionosphere-free constraint)} \tag{2.10}$$

$$\sum_i c_i = 1 \qquad \text{(geometry-estimator constraint)} \tag{2.11}$$

$$\sum_i -\frac{\kappa_u}{f_i^2} c_i = 1 \qquad \text{(TECu-estimator constraint)} \tag{2.12}$$

The geometry-free and ionosphere-free constraints are named because they effectively remove the G and I_i terms in the resultant combination. The geometry-estimator and TECu-estimator constraints are named because they produce the terms G and TECu, respectively, with unity coefficients in the resultant combination. The intention here is to introduce constraints that can be applied together in order to achieve particular linear estimation objectives, so long as they are consistent (e.g. note that simultaneously removing the geometry and estimating geometry are contradictory objectives).

2.3.2 Homogeneous Versus Non-Homogeneous Constraints

An important distinction between these constraints is that the geometry-free and ionosphere-free constraints are homogeneous, while the estimator constraints are non-homogeneous. Applying homogeneous constraints will restrict valid coefficient vectors to lie in an $m-1$ dimensional subspace of $\mathbb{R}^m$. This means that successive applications of distinct homogeneous constraints will cause a corresponding decrease in the maximum size of a linearly independent set of coefficient vectors. In contrast, the non-homogeneous constraints restrict valid coefficient vectors to lie in an affine hyperplane. Figure 2.1 illustrates this concept for two-dimensional hyperplanes in a three-dimensional linear space.

2.3.3 Linear Combination Error Reduction Criteria

In addition to coefficient constraints that estimate or remove the geometry and TEC model parameters, we may choose linear combination coefficients to optimally reduce systematic error or stochastic error variance. Recalling Equation 2.7 for the bound on systematic

error in the linear combination, we define the following coefficient vector criterion for optimal reduction of maximum systematic error:

$$\mathbf{C}^* = \arg\min_{\mathbf{C}} \sum_i |c_i| \ |S_i|_{\max} \tag{2.13}$$

For the case that the systematic error bound is the same for each signal, this criterion simplifies to:

$$\mathbf{C}^* = \arg\min_{\mathbf{C}} \sum_i |c_i| \tag{2.14}$$

(a) Hyperplane for homogeneous constraint. (b) Hyperplane for non-homogeneous constraint.

Figure 2.1: Geometry-free and ionosphere-free constraints are homogeneous and their valid coefficients will lie within a linear subspace. Estimator constraints are non-homogeneous and their valid coefficients lie in a hyperplane that is not a linear subspace.

Similarly, recalling Equation 2.8 for the linear combination stochastic error variance, we define the following criterion for optimal reduction of stochastic error:

$$\mathbf{C}^* = \ \arg\min_{\mathbf{C}} \mathbf{C}^T \Sigma_\epsilon \mathbf{C} \tag{2.15}$$

For the case that ϵ_i are uncorrelated and of equal amplitude, this criterion simplifies to:

$$\mathbf{C}^* = \ \arg\min_{\mathbf{C}} \langle \mathbf{C} | \mathbf{C} \rangle \ = \ \arg\min_{\mathbf{C}} \sum_i c_i^2 \tag{2.16}$$

2.4 TEC Estimators

We now turn our attention to the use of these constraints and criteria in order to estimate our model parameters. As the focus of our work, we first introduce TEC estimators, which we define to be a set of coefficients that satisfy the TECu-estimator constraint in Equation 2.12. In the context of multi-frequency GNSS, there is a large set of possible TEC estimator coefficients, and in general their optimality depends upon a priori information about our model and observations. With no further information other than that $|G| \gg |I_i| \gg |S_i|$, a good TEC estimator should satisfy the geometry-free constraint in Equation 2.9. We call such coefficients geometry-free TEC estimators.

2.4.1 TEC Estimators for Triple-Frequency GNSS

In the context of triple-frequency GNSS ($m = 3$), applying the geometry-free and ionosphere-estimator constraints yields the following system of coefficients with one degree of freedom (denoted by x):

$$\begin{aligned} c_1 &= \frac{\frac{1}{\kappa_u} + x\left(\frac{1}{f_3^2} - \frac{1}{f_2^2}\right)}{\frac{1}{f_2^2} - \frac{1}{f_1^2}} \\ c_2 &= \frac{-\frac{1}{\kappa_u} - x\left(\frac{1}{f_3^2} - \frac{1}{f_1^2}\right)}{\frac{1}{f_2^2} - \frac{1}{f_1^2}} \\ c_3 &= x \end{aligned} \tag{2.17}$$

We can choose $\mathbf{C}$ using the criteria to reduce either the maximum systematic error or the stochastic error variance. First we consider the simple case of the maximum systematic error reduction criterion given in Equation 2.14. The optimal coefficients must lie at one of the critical points of the objective function $\sum_i |c_i|$, which occur where any of c_i have a zero-crossing. For triple-frequency GNSS, this occurs at the zero-crossing of the coefficient

corresponding to the middle-frequency signal, so that the optimal TEC estimator is that which uses only two observations with the widest possible frequency spacing. E.g. if $f_1 > f_2 > f_3$, then $c_2 = 0$ and the remaining coefficients are determined by Equation 2.17.

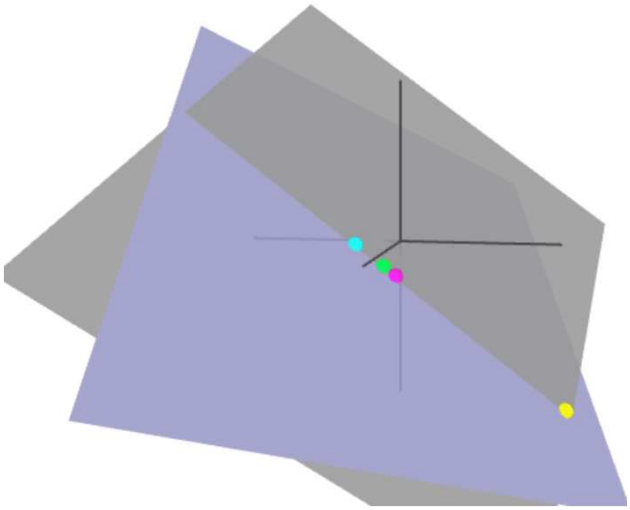

Figure 2.2: For triple-frequency GPS signals, shows the intersection of the geometry-free subspace (gray plane) and the TECu-estimator hyperplane (gray plane). Also shows coefficients for TEC estimates $\text{TEC}_{\text{L1,L2,L5}}$ (green dot), $\text{TEC}_{\text{L1,L5}}$ (pink dot), $\text{TEC}_{\text{L1,L2}}$ (cyan dot), and $\text{TEC}_{\text{L2,L5}}$ (yellow dot).

Next we consider the simple case of the stochastic error variance reduction criterion given in Equation 2.16. The quadratic objective function $\sum_i c_i^2$ can be minimized with respect to x. The value of x that minimizes this objective function is given by:

$$x^* = \frac{\frac{1}{\kappa_u}\left(\frac{2}{f_3^2} - \frac{1}{f_2^2} - \frac{1}{f_1^2}\right)}{\left(\frac{1}{f_1^2} - \frac{1}{f_2^2}\right)^2 + \left(\frac{1}{f_2^2} - \frac{1}{f_3^2}\right)^2 + \left(\frac{1}{f_3^2} - \frac{1}{f_1^2}\right)^2} \tag{2.18}$$

Substituting x^* back into Equation 2.17, we obtain triple-frequency geometry-free TEC estimator with minimum sum-of-squares coefficients, which we denote $\mathbf{C}_{\text{TEC}_{1,2,3}}$ (where 1, 2, and 3 represent the three relevant signals).

2.4.2 Important Properties of Triple-Frequency TEC Estimators

Consider the fact that any triple-frequency geometry-free TEC estimator lies on a line that is the intersection of the geometry-free and TECu-estimator constraint hyperplanes, as

shown in Figure 2.2. An important consequence of this fact is that given two different TEC estimators $\mathbf{C}_{\mathrm{TEC}_1}$ and $\mathbf{C}_{\mathrm{TEC}_2}$, any third TEC estimator can be expressed as:

$$\mathbf{C}_{\mathrm{TEC}} = \mathbf{C}_{\mathrm{TEC}_1} + \alpha \left(\mathbf{C}_{\mathrm{TEC}_2} - \mathbf{C}_{\mathrm{TEC}_1} \right) \tag{2.19}$$

for some constant α.

Also consider the estimator $\mathbf{C}_{\mathrm{TEC}_{1,2,3}}$, which, because it has minimum sum-of-squares coefficients, is the closest point on the line to the origin. The projection of any geometry-free TEC estimator onto the span of $\mathbf{C}_{\mathrm{TEC}_{1,2,3}}$ will land directly at $\mathbf{C}_{\mathrm{TEC}_{1,2,3}}$. It follows that, for any triple-frequency geometry-free TEC estimator $\mathbf{C}_{\mathrm{TEC}}$, we have:

$$\frac{\langle \mathbf{C}_{\mathrm{TEC}_{1,2,3}} | \mathbf{C}_{\mathrm{TEC}} \rangle}{||\mathbf{C}_{\mathrm{TEC}_{1,2,3}}||} = ||\mathbf{C}_{\mathrm{TEC}_{1,2,3}}|| \tag{2.20}$$

2.4.3 TEC Estimators for Triple-Frequency GPS

Here we consider the geometry-free TEC estimators for triple-frequency GPS signals. Let frequencies f_1, f_2 and f_3 correspond to GPS signals L1, L2, and L5 respectively. Figure 2.3 depicts the system in Equation 2.17 (parameterized along the x-axis) for geometry-free TEC estimators applied to GPS signal frequencies. Along with the coefficient values, the figure also shows sum-of-squares and sum-of-absolute-value characteristics.

Table 2.1: Notable coefficients for triple-frequency GPS TEC estimators along with their sum-of-squares and sum-of-absolute-value characteristics.

GPS TEC Estimator Coefficients

Estimate	L1CA	L2C	L5	$\sum_i c_i^2$	$\sum_i \lvert c_i \rvert$
$\mathrm{TEC}_{\mathrm{L1,L2,L5}}$	8.294	-2.883	-5.411	10.314	16.588
$\mathrm{TEC}_{\mathrm{L1,L5}}$	7.762	0	-7.762	10.977	15.524
$\mathrm{TEC}_{\mathrm{L1,L2}}$	9.518	-9.518	0	13.460	19.035
$\mathrm{TEC}_{\mathrm{L2,L5}}$	0	42.080	-42.080	59.510	84.160

There are four notable sets of coefficients that we consider; they are shown along with their sum-of-squares and sum-of-absolute-values in Table 2.1. The first satisfies the simplified stochastic error reduction criterion (i.e. it is the minimizer of sum-of-squares). This estimator

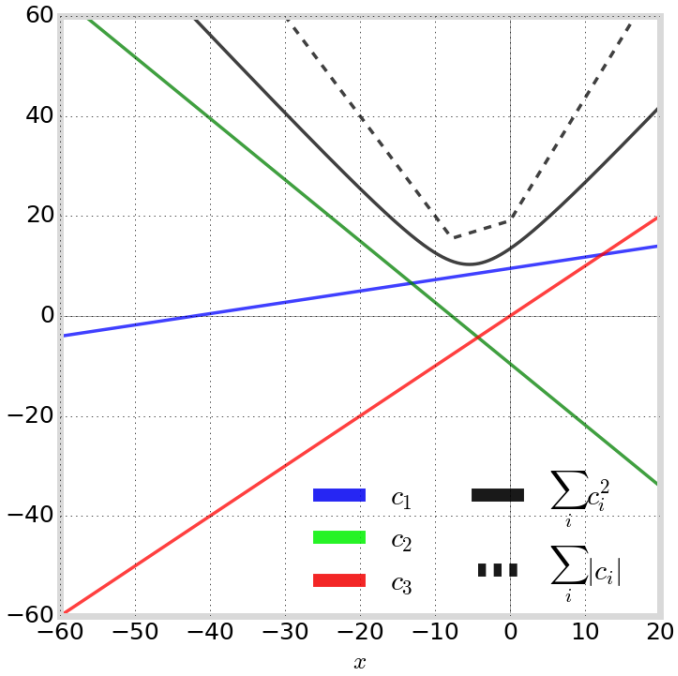

Figure 2.3: The system of possible coefficients for a good TEC estimator, parameterized along the x-axis. The coefficients' sum-of-squares is shown in solid black and their sum-of-absolute-value is shown in dashed black.

has nonzero coefficients for each signal, and so we denote its corresponding TEC estimate $\text{TEC}_{\text{L1,L2,L5}}$. The next set of coefficients are the nominal dual-frequency TEC estimator coefficients using L1 and L5, whose estimate we denote $\text{TEC}_{\text{L1,L5}}$. As discussed above, these coefficients satisfy the simplified maximum systematic error reduction criterion since f_1 and f_3 corresponding to signals L1 and L5 have the widest frequency spacing ($f_1 > f_2 > f_3$). The remaining estimators are the nominal dual-frequency estimators using signal pairs L1/L2 and L2/L5. We denote their corresponding TEC estimates as $\text{TEC}_{\text{L1,L2}}$ and $\text{TEC}_{\text{L2,L5}}$ respectively.

2.5 Geometry Estimators

A geometry estimator is a set of coefficients that satisfy the geometry-estimator constraint in Equation 2.11. Similar to our analysis for TEC estimators, applying the knowledge that $|G| \gg |I_i| \gg |S_i|$ suggests that good geometry estimator coefficients should satisfy the ionosphere-free constraint. We call such coefficients ionosphere-free geometry estimators. Such combinations are widely used in conventional dual-frequency GNSS processing. The author in [25] presents both dual-frequency and triple-frequency ionosphere-free phase combinations that estimate the geometry term. The results we present here match those found in that work.

2.5.1 Geometry Estimators for Triple-Frequency GNSS

Applying the ionosphere-free and geometry-estimator constraints yields the following system of coefficients with one degree of freedom (denoted by x):

$$\begin{aligned} c_1 &= \frac{-\frac{1}{f_2^2} + x\left(\frac{1}{f_2^2} - \frac{1}{f_3^2}\right)}{\frac{1}{f_1^2} - \frac{1}{f_2^2}} \\ c_2 &= \frac{\frac{1}{f_1^2} - x\left(\frac{1}{f_1^2} - \frac{1}{f_3^2}\right)}{\frac{1}{f_1^2} - \frac{1}{f_2^2}} \\ c_3 &= x \end{aligned} \tag{2.21}$$

Again, we can choose $\mathbf{C}$ using the criteria to reduce either the maximum systematic error or the stochastic error variance. With regards to the simplified maximum systematic error reduction criterion given in Equation 2.14, we again find that using only two signals with the widest frequency spacing provides the best estimate.

For the case of the simplified stochastic error variance reduction criterion given in Equation 2.16, we can again solve for x to minimize the objective function $\sum_i c_i^2$. The value of x that minimizes this objective function is given by:

$$x^* = \frac{\frac{1}{f_1^4} + \frac{1}{f_2^4} - \frac{1}{f_3^2}\left(\frac{1}{f_1^2} - \frac{1}{f_2^2}\right)}{\left(\frac{1}{f_1^2} - \frac{1}{f_2^2}\right)^2 + \left(\frac{1}{f_2^2} - \frac{1}{f_3^2}\right)^2 + \left(\frac{1}{f_1^2} - \frac{1}{f_3^2}\right)^2} \tag{2.22}$$

Substituting x^* back into Equation 2.21, we obtain the triple-frequency ionosphere-free geometry estimator with minimum sum-of-squares coefficients, which we denote $\mathbf{C}_{G_{1,2,3}}$. The important properties laid out in Section 2.4.2 are analogous for geometry estimators.

2.5.2 Geometry Estimators for Triple-Frequency GPS

Here we consider the ionosphere-free geometry estimators for triple-frequency GPS signals. Once again, let frequencies f_1, f_2 and f_3 correspond to GPS signals L1, L2, and L5. Figure 2.4 depicts the system in Equation 2.21 (parameterized along the x-axis) for ionosphere-free geometry estimators applied to GPS frequencies. The figure shows the coefficient values along with the sum-of-squares and sum-of-absolute-value characteristics.

It is interesting to note the similarity between figures 2.3 and 2.4. Since the orientations of the geometry-free with TECu-estimator and the ionosphere-free with geometry-estimator hyperplanes are identical, their corresponding intersections are parallel lines. As each system was parameterized by its third component, their depiction in two dimensions will look identical except for a difference in scaling of the axes.

Similar to our analysis of triple-frequency GPS TEC estimators, there are four notable sets of coefficients for triple-frequency GPS geometry estimators. Table 2.1 shows these coefficients along with their sum-of-squares and sum-of-absolute-values. The first satisfies

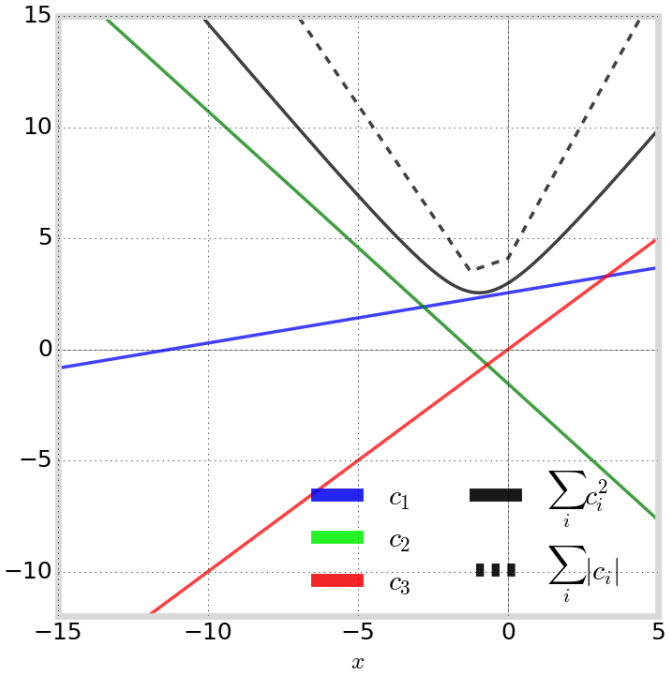

Figure 2.4: The system of possible coefficients for ionosphere-free geometry estimators, parameterized along the x-axis. The coefficients' sum-of-squares is shown in solid black and their sum-of-absolute-value is shown in dashed black.

Table 2.2: Notable coefficients for triple-frequency GPS geometry estimators along with their sum-of-squares and sum-of-absolute-value characteristics.

GPS Geometry Estimator Coefficients

Estimate	L1CA	L2C	L5	$\sum_i c_i^2$	$\sum_i \lvert c_i \rvert$
$G_{\mathrm{L1,L2,L5}}$	2.327	-0.360	-0.967	2.546	3.654
$G_{\mathrm{L1,L5}}$	2.261	0	-1.261	2.588	3.522
$G_{\mathrm{L1,L2}}$	2.546	-1.546	0	2.978	4.091
$G_{\mathrm{L2,L5}}$	0	12.255	-11.255	16.639	23.510

the simplified stochastic error reduction criterion. This estimator has nonzero coefficients for each signal, and we denote its corresponding estimate $G_{\mathrm{L1,L2,L5}}$. The next set of coefficients use only signals L1 and L5, and we denote its estimate as $G_{\mathrm{L1,L5}}$. These coefficients satisfy the simplified maximum systematic error reduction criterion. The remaining estimators use signal pairs L1/L2 and L2/L5, and we denote their corresponding estimates $G_{\mathrm{L1,L2}}$ and $G_{\mathrm{L2,L5}}$ respectively.

2.6 Estimation of Systematic Errors

Here we discuss estimation of systematic errors S_i. With our only a priori knowledge being $|G| \gg |I_i| \gg |S_i|$, it is apparent that estimators of systematic errors should apply both the geometry-free and ionosphere-free constraints. If we choose to estimate a particular systematic error S_j, it also makes sense to apply $c_j = 1$ as a constraint – i.e. apply the relevant systematic-error estimator constraint. As before, we can then optimize among valid coefficient vectors to minimize the maximum impact of remaining systematic errors or to minimize stochastic error variance.

2.6.1 Systematic Error Estimation in Triple-Frequency GNSS

In the context of triple-frequency GNSS signals, applying the geometry-free and ionosphere-free constraints yields the following system of coefficients with one degree of freedom (denoted by x):

$$\begin{aligned} c_1 &= x\frac{\frac{1}{f_3^2} - \frac{1}{f_2^2}}{\frac{1}{f_2^2} - \frac{1}{f_1^2}} \\ c_2 &= -x\frac{\frac{1}{f_3^2} - \frac{1}{f_1^2}}{\frac{1}{f_2^2} - \frac{1}{f_1^2}} \\ c_3 &= x \end{aligned} \tag{2.23}$$

Note that the set of coefficients satisfying Equation 2.23 lie in a one-dimensional linear subspace of $\mathbb{R}^3$. This is expected since we applied two unique linear homogeneous constraints.

As a result, there is one signal – unique up to some scaling – that contains information about systematic errors S_i. We call this signal the geometry-ionosphere-free combination (GIFC).

The choice of scaling for the triple-frequency GIFC is arbitrary since the systematic error components will always appear in the same proportion. As such, it does not make sense to apply the constraint $c_j = 1$ when trying to estimate S_j. Rather, the GIFC must be viewed as the single available indicator of systematic errors. There is no way to further separate residuals due to S_1 versus S_2, etc. using linear estimators.

2.6.2 Important Properties of Triple-Frequency GIFC Coefficients

Here we describe some important properties regarding the triple-frequency GIFC coefficients. First, we note that the span of $\mathbf{C}_{\text{GIFC}}$ has the same orientation as the line of triple-frequency geometry-free TEC estimators, as shown in Figure 2.5. To see why, consider the difference between any two TEC estimators $\mathbf{C}_{\text{TEC}_1} - \mathbf{C}_{\text{TEC}_2}$. In their resulting combination, the term containing TECu goes to zero and is therefore ionosphere-free. It follows that $\mathbf{C}_{\text{TEC}_1} - \mathbf{C}_{\text{TEC}_2}$ must correspond to some scaling of geometry-ionosphere-free coefficients:

$$\mathbf{C}_{\text{GIFC}} = \alpha \left(\mathbf{C}_{\text{TEC}_1} - \mathbf{C}_{\text{TEC}_2} \right) \tag{2.24}$$

where α depends on the scaling of $\mathbf{C}_{\text{GIFC}}$.

Additionally, we note that $\mathbf{C}_{\text{GIFC}}$ is orthogonal to the triple-frequency geometry-free TEC estimator coefficients $\mathbf{C}_{\text{TEC}_{1,2,3}}$:

$$\langle \mathbf{C}_{\text{GIFC}} | \mathbf{C}_{\text{TEC}_{1,2,3}} \rangle = 0 \tag{2.25}$$

As a consequence, the GIFC provides no direct information on the residual errors present in the corresponding estimation $\text{TEC}_{1,2,3}$ whose error signal lies in the null space of the GIFC estimator.

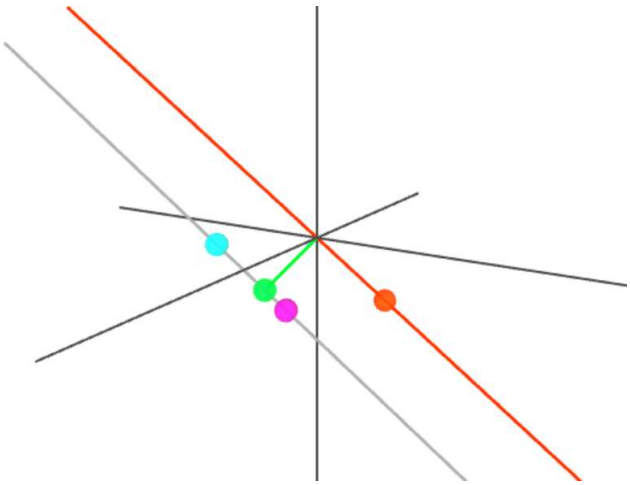

Figure 2.5: For triple-frequency GPS signals, shows the GIFC subspace and coefficients (orange line and dot). Also shows coefficients for TEC estimates $\mathrm{TEC}_{\mathrm{L1,L2,L5}}$ (green dot), $\mathrm{TEC}_{\mathrm{L1,L5}}$ (pink dot), and $\mathrm{TEC}_{\mathrm{L1,L2}}$ (cyan dot), along with the line corresponding to all geometry-free TEC estimators (gray line). The green line corresponding to $\mathbf{C}_{\mathrm{TEC}_{\mathrm{L1,L2,L5}}}$ is orthogonal to the orange line.

2.6.3 Systematic Error Estimation in Triple-Frequency GPS

When dealing with triple-frequency GPS signals, we choose to use a GIFC scaling whose corresponding coefficients are:

$$\mathbf{C}_{\mathrm{GIFC}_{\mathrm{L1,L2,L5}}} = [-1.756, 9.520, -7.764]^T \tag{2.26}$$

This scaling is chosen so that $\mathbf{C}_{\mathrm{GIFC}_{\mathrm{L1,L2,L5}}} = \mathbf{C}_{\mathrm{TEC}_{\mathrm{L1,L5}}} - \mathbf{C}_{\mathrm{TEC}_{\mathrm{L1,L2}}}$ and thus $\mathrm{GIFC}_{\mathrm{L1,L2,L5}} = \mathrm{TEC}_{L1,L5} - \mathrm{TEC}_{L1,L2}$. A convenient aspect of this scaling is that its norm is very close to the norm of $\mathrm{TEC}_{\mathrm{L1,L2}}$.

2.7 Residual Errors in TEC Estimates

One of our goals in observing the GIFC is to quantify the impact of residual errors (i.e. the S_i and ϵ_i terms) on TEC estimates. Let us define the error residual vector $\mathbf{R}$ with components R_i corresponding to signals Φ_i:

$$R_i = S_i + \epsilon_i \tag{2.27}$$

Given a set of TEC estimator coefficients $\mathbf{C}_{\text{TEC}}$, the residual error impacting the TEC estimate is:

$$R_{\text{TEC}} = \langle \mathbf{C}_{\text{TEC}} | \mathbf{R} \rangle \tag{2.28}$$

Note that the residual error shown in the GIFC is itself:

$$\text{GIFC} = R_{\text{GIFC}} = \langle \mathbf{C}_{\text{GIFC}} | \mathbf{R} \rangle \tag{2.29}$$

We would like to express the residual error for TEC estimates in a convenient basis related to the GIFC and optimal triple-frequency TEC estimator that we derived earlier. Recalling from Section 2.6.2 that $\mathbf{C}_{\text{TEC}_{1,2,3}}$ is orthogonal to $\mathbf{C}_{\text{GIFC}}$, we define the orthonormal basis:

$$\begin{aligned} \mathbf{U}_1 &= \frac{\mathbf{C}_{\text{GIFC}}}{||\mathbf{C}_{\text{GIFC}}||} \\ \mathbf{U}_2 &= \frac{\mathbf{C}_{\text{TEC}_{1,2,3}}}{||\mathbf{C}_{\text{TEC}_{1,2,3}}||} \\ \mathbf{U}_3 &= \mathbf{U}_1 \times \mathbf{U}_2 \end{aligned} \tag{2.30}$$

We can decompose $\mathbf{R}$ into its components R'_i in this new basis:

$$R'_i = \langle \mathbf{U}_i | \mathbf{R} \rangle \qquad \text{for } i \in \{1, 2, 3\} \tag{2.31}$$

Since $\mathbf{U}_1$ and $\mathbf{U}_2$ span the geometry-free subspace, we can decompose any set of geometry-free TEC estimator coefficients $\mathbf{C}_{\text{TEC}}$ with respect to just $\mathbf{U}_1$ and $\mathbf{U}_2$ to obtain:

$$\mathbf{C}_{\text{TEC}} = \langle \mathbf{U}_1 | \mathbf{C}_{\text{TEC}} \rangle \mathbf{U}_1 + \langle \mathbf{U}_2 | \mathbf{C}_{\text{TEC}} \rangle \mathbf{U}_2 \tag{2.32}$$

The corresponding error residual is then:

$$R_{\text{TEC}} = \langle \mathbf{U}_1 | \mathbf{C}_{\text{TEC}} \rangle R'_1 + \langle \mathbf{U}_2 | \mathbf{C}_{\text{TEC}} \rangle R'_2 \tag{2.33}$$

Now using the property $\frac{\langle \mathbf{C}_{\text{TEC}_{1,2,3}} | \mathbf{C}_{\text{TEC}} \rangle}{||\mathbf{C}_{\text{TEC}_{1,2,3}}||} = ||\mathbf{C}_{\text{TEC}_{1,2,3}}||$ from Equation 2.20, we have that $\langle \mathbf{U}_2 | \mathbf{C}_{\text{TEC}} \rangle = ||\mathbf{C}_{\text{TEC}_{1,2,3}}||$ for any TEC estimator $\mathbf{C}_{\text{TEC}}$. Expanding the terms for $\mathbf{U}_1$ and $\mathbf{U}_2$, the expression for residual error in the TEC estimate can be written:

$$
\begin{aligned}
R_{\text{TEC}} = \; & \langle \mathbf{U}_1 | \mathbf{C}_{\text{TEC}} \rangle R'_1 + ||\text{TEC}_{1,2,3}|| R'_2 \\
= \; & \frac{\langle \mathbf{C}_{\text{GIFC}} | \mathbf{C}_{\text{TEC}} \rangle}{||\mathbf{C}_{\text{GIFC}}||^2} R_{\text{GIFC}} + R_{\text{TEC}_{1,2,3}}
\end{aligned} \tag{2.34}
$$

This shows that, in essence, there are two components to the residual errors that affect TEC estimations. The first component R'_1 is in the direction of $\mathbf{C}_{\text{GIFC}}$ and is observable through the GIFC. The second component R'_2 is in the direction of $\mathbf{C}_{\text{TEC}_{1,2,3}}$ and is unobservable. R'_2 can be thought of as the residual error that behaves like TEC, while R'_1 is the component that behaves exactly unlike TEC. The third residual error component R'_3 does not affect TEC estimates.

By observing diverse measurements of the GIFC, we can construct an overall distribution R_{GIFC}, which scales by $\frac{1}{||\mathbf{C}_{\text{GIFC}}||}$ to form the distribution of R'_1. Then, the deviations of the distribution of R'_1 can be related to deviations in the residuals of different TEC estimations using the factor $\langle \mathbf{C}_{\text{GIFC}} | \mathbf{C}_{\text{TEC}} \rangle / ||\mathbf{C}_{\text{GIFC}}||$. It is also useful to consider the factor $\langle \mathbf{C}_{\text{GIFC}} | \mathbf{C}_{\text{TEC}} \rangle / ||\mathbf{C}_{\text{GIFC}}||^2$, which directly relates deviations in R_{GIFC} to R_{TEC}. Table 2.3 shows both of these quantities for the triple-frequency GPS geometry-free TEC estimators from Table 2.1, where $\mathbf{C}_{\text{GIFC}}$ is taken to be $\mathbf{C}_{\text{GIFC}_{\text{L1,L2,L5}}}$ from Equation 2.26.

Table 2.3: Shows the quantities $\frac{\langle \mathbf{C}_{\text{GIFC}} | \mathbf{C}_{\text{TEC}} \rangle}{||\mathbf{C}_{\text{GIFC}}||}$, $\frac{\langle \mathbf{C}_{\text{GIFC}} | \mathbf{C}_{\text{TEC}} \rangle}{||\mathbf{C}_{\text{GIFC}}||^2}$, and $\frac{||\mathbf{C}_{\text{TEC}}||}{||\mathbf{C}_{\text{GIFC}}||}$ for each of the significant triple-frequency GPS geometry-free TEC estimators from Table 2.1. $\mathbf{C}_{\text{GIFC}}$ is taken to be $\mathbf{C}_{\text{GIFC}_{\text{L1,L2,L5}}}$

Estimate	$\frac{\langle \mathbf{C}_{\text{GIFC}} \vert \mathbf{C}_{\text{TEC}} \rangle}{\vert\vert \mathbf{C}_{\text{GIFC}} \vert\vert}$	$\frac{\langle \mathbf{C}_{\text{GIFC}} \vert \mathbf{C}_{\text{TEC}} \rangle}{\vert\vert \mathbf{C}_{\text{GIFC}} \vert\vert^2}$	$\frac{\vert\vert \mathbf{C}_{\text{TEC}} \vert\vert}{\vert\vert \mathbf{C}_{\text{GIFC}} \vert\vert}$
$\text{TEC}_{\text{L1,L2,L5}}$	0	0	0.831
$\text{TEC}_{\text{L1,L5}}$	3.758	0.303	0.885
$\text{TEC}_{\text{L1,L2}}$	-8.649	-0.697	1.085
$\text{TEC}_{\text{L2,L5}}$	58.610	4.723	4.796

At this point, we want to make some useful claim about the overall residual error R_{TEC} impacting TEC estimates, but we only have information on one component R'_1 that affects them. In order continue, we must start making additional assumptions and claims about the systematic error components S_i. Up until now, we have assumed that they are small

compared to the G and I terms in our model, but we have not said anything about the relationship between the individual error components R_i.

Let us consider R_i as random variables whose overall joint distribution is symmetric about the origin. In a rough sense, this treats the individual error components for each R_i as independent and of equal amplitude. While this assumption is certainly not accurate with regards to real triple-frequency GNSS signals, it allows for more insightful analysis and more useful comparison between TEC estimators. If this is the case, then the distribution in GIFC can be used to approximate the distribution of residual errors any TEC estimate. In this case, the scaling factor relating deviations in the GIFC to approximated deviations in TEC is simply the ratio of their coefficient norms, or $\frac{||\mathbf{C}_{\text{TEC}}||}{||\mathbf{C}_{\text{GIFC}}||}$. This quantity is also provided in Table 2.3 for the relevant GPS TEC estimators.

CHAPTER 3: APPLICATION AND RESULTS

In this section, we apply the theory on GIFC to real GPS data. We will discuss the nature of our data and how it was obtained. Then we will discuss the processing steps used to compute and level the GIFC over many datasets. Finally, we present results and interpretation of computed GIFC signals.

3.1 Data Collection

For our analysis, we obtain data from a high-rate GNSS data collection network [28]. Figure 3.1 shows the sites that are part of the receiver network. For the work presented here, we use data from receivers at Jicimarca, Poker Flat, and Hok Tsui. Each site is equipped with at least one Septentrio PolaRxS scintillation monitoring receiver. These receivers are configured to record all available GNSS constellations and signals. Recorded measurements are stored in a proprietary format called Septentrio Binary Format (SBF).

For our work, we are interested in GPS signals L1CA, L2C, and L5. We choose to look at data from GPS satellites G01, G24, G25, and G27, as each of these satellites has been transmitting triple-frequency signals since at least 2013 (see Figure 1.5). For our analysis, we use data ranging from 2013-01-01 through 2016-04-26. However, due to data outages and processing anomalies, we end up analyzing data from approximately two-thirds of the days in this time period.

3.2 Data Processing Overview

In Figure 3.2 we depict the data-processing steps taken in order to produce analyzable results. The first step is to extract the relevant measurements from the SBF files used to archive the data. These include time series of the phase measurements from each satellite of interest. Next, we combine extracted phase measurement time series from a given satellite using the coefficients from Equation 2.26 to form the GIFC signal. Then, we align and level

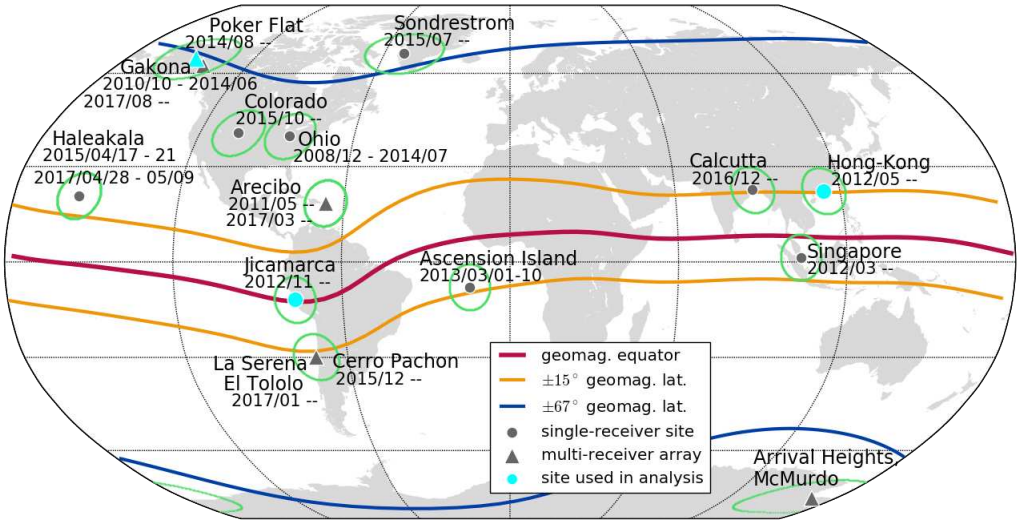

Figure 3.1: Map of GNSS data collection sites. Each site is equipped with a Septentrio PolaRxS scintillation monitoring receiver. The sites whose data we use in this work are marked in cyan.

the GIFC signals, run a jump correction algorithm, and perform an integrity check. Finally, we aggregate and visualize the results. In the remainder of this section, we describe each processing steps in detail.

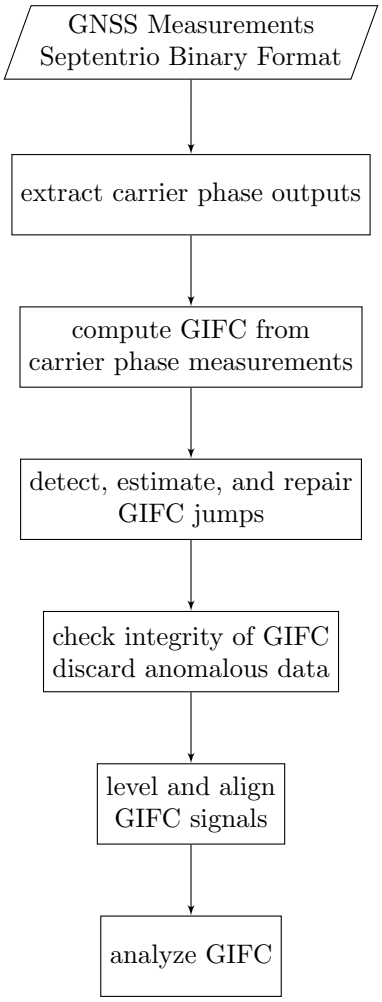

Figure 3.2: Data processing block diagram that shows the data-processing steps taken to convert SBF files into analyzable results.

3.2.1 Pass Alignment

Recall from Section 1.2.1 that GPS satellites have orbital periods of roughly one-half sidereal day. To a static receiver on the ground, the satellite will pass through the same part of the sky approximately every 23 hours and 58 minutes. As such, the satellite-receiver geometry is nearly identical each day, and the pattern of systematic errors in the GIFC looks

very similar. In actuality, the orbital period is slightly different and changes slowly for each satellite. The mean orbital period must be estimated in order to reasonably align data over a multi-year period.

In order to align the GIFC signal for consecutive passes, we first choose a reference epoch (2013-01-01) and define a "pass period" as one sidereal day. Then, we apply a shift according to the number of pass periods that have elapsed between the reference epoch and the signal measurement times. We adjust the pass period until the total shift between the first and last available data appears to be at least less than 5 minutes, based off of day-to-day correlation in the GIFC shape. For the satellites used in our analysis, the mean pass periods tend to be around 7 seconds shorter than the mean sidereal day.

Finally, we note that the data we use is archived in 24-hour datasets, and sometimes a single pass overlaps two datasets. If this is the case, the two datasets are merged so the pass can be considered as a whole.

3.2.2 Jumps in GIFC Data

For our analysis dealing with 1 Hz measurements, it is often the case that receiver loss-of-lock and interference/ionosphere-induced rapid phase changes, or "cycle-slips," can cause jumps in the carrier ambiguity term λN from Equation 1.10. This causes a corresponding jump in the GIFC. For interference/ionosphere-induced cycle slips, the underlying cause is due to deep fades in the signal intensity that allow noise to disrupt receiver phase-lock. These slips can occur for any satellite at any point during the pass, but are usually associated with strong ionosphere activity, interference, or multipath at low elevations. We correct for cycle slips when possible, though some datasets such as in Figure 3.4 are beyond the correction capabilities of the simple method we present here.

The method for correction of GIFC jumps simultaneously addresses loss-of-lock and cycle-slip related jumps. First, we take the epoch-to-epoch difference of the GIFC signal and identify all segments in which we are confident that jumps did not occur, that is, segments

where the epoch-to-epoch difference remains less than 0.2 for the relevant GIFC scaling. To each segment we ascribe a bias value. Then, we simultaneously estimate the bias values with a 5th-order polynomial fit to the GIFC. The implementation of this linear fit and bias estimation is given in Appendix AB. We use the bias value estimates to correct the GIFC signal. Figure 3.3 shows an example of the GIFC before and after jump correction.

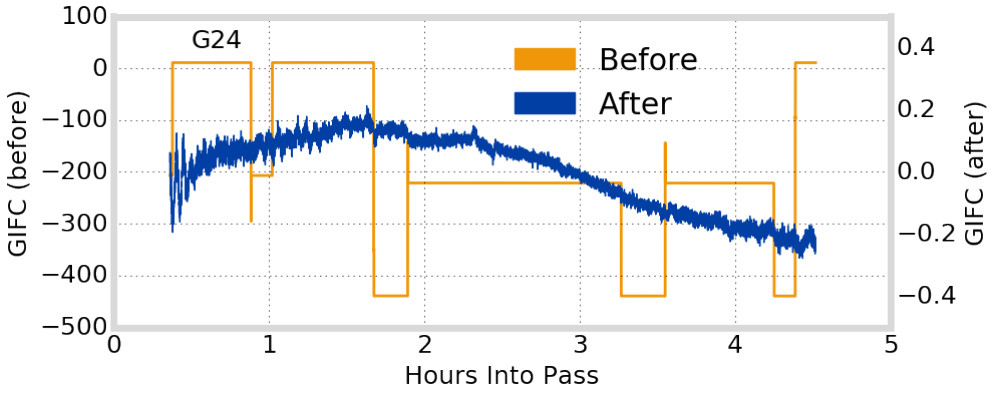

Figure 3.3: Shows example of GIFC jump correction before (orange) and after (blue) applying our correction algorithm.

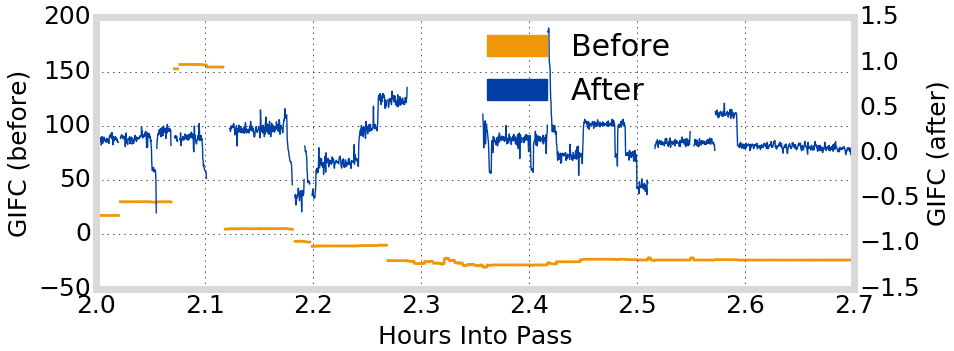

Figure 3.4: Shows example of a pass with many jumps in short succession likely due to ionosphere-induced cycle slips. Our jump correction algorithm was insufficient to correct the GIFC for this example.

3.2.3 Anomalous Datasets

Anomalous datasets occur when our jump correction algorithm fails or some other event causes the GIFC signal to have very large variation in magnitude. To check whether a

dataset is valid, we level the GIFC to zero using its value at the epoch closest to that of the satellite's highest elevation. Then, if the absolute value of the GIFC is larger than 1.5, the data is considered anomalous. If the satellite elevation is also below 20° during the portions of the signal that are above the threshold, then just those portions are removed from our analysis. Otherwise the entire dataset is removed. Figure 3.4 shows a case where jump correction failed and the dataset was removed from analysis.

3.3 Results

In this section, we show results pertaining to the GIFC. The goal is to characterize the nature of the GIFC for triple-frequency GPS and to analyze the nature of the underlying systematic errors it exposes. We begin with normal examples of the GIFC signal for single passes, then move on to exploring patterns in the GIFC signals. Ultimately, we relate deviation percentiles for GIFC signals to estimated deviation percentiles for the error residuals in TEC estimates, which is the key contribution of this work.

3.3.1 GIFC Examples

For satellites G01, G24, G25, and G27, figures 3.5, 3.6, and 3.7 show nominal examples of the GIFC during quiet days for receivers in Poker Flat, Hok Tsui, and Jicamarca respectively. The satellite elevation is also shown. The most prominent features are the large-scale trends that occur over the entire pass and the multipath fluctuations. Stochastic noise also appears largest near the ends of the satellite passes. We should note that, because of its high latitude, the receiver in Poker Flat, Alaska actually observes two passes daily for a given satellite, but here we only show the longest pass.

3.3.2 Multi-Year GIFC Variations

Figures 3.8, 3.9, and 3.10 show how the GIFC changes over the course of 3 years for receivers in Poker Flat, Hok Tsui, and Jicamarca respectively. The images reveal that the large-scale trend in the GIFC is relatively static from day to day but changes slowly over a

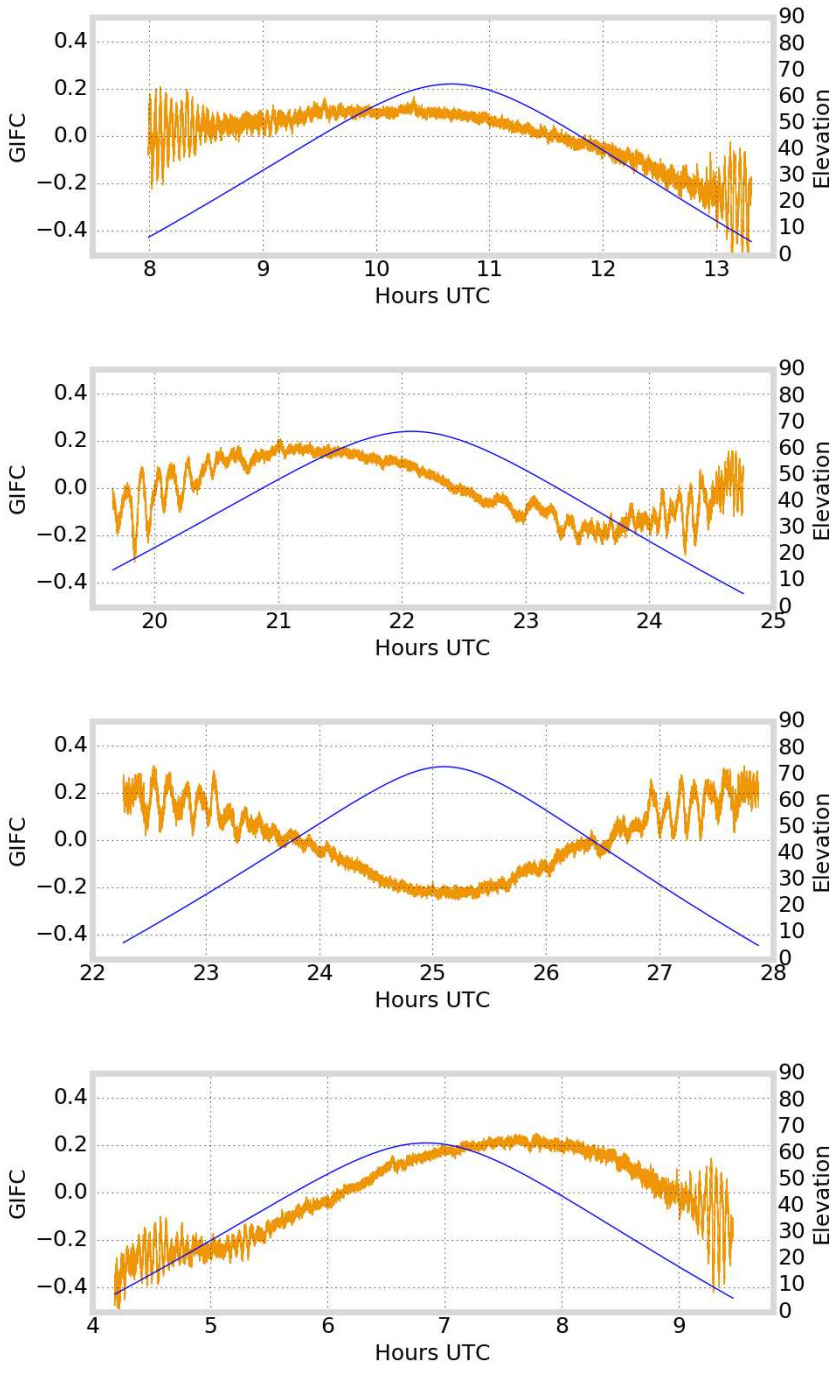

Figure 3.5: Shows nominal GIFC (orange line) of satellites G01, G24, G25, and G27 during quiet day for a receiver at Poker Flat, Alaska. Satellite elevation is also shown (blue line).

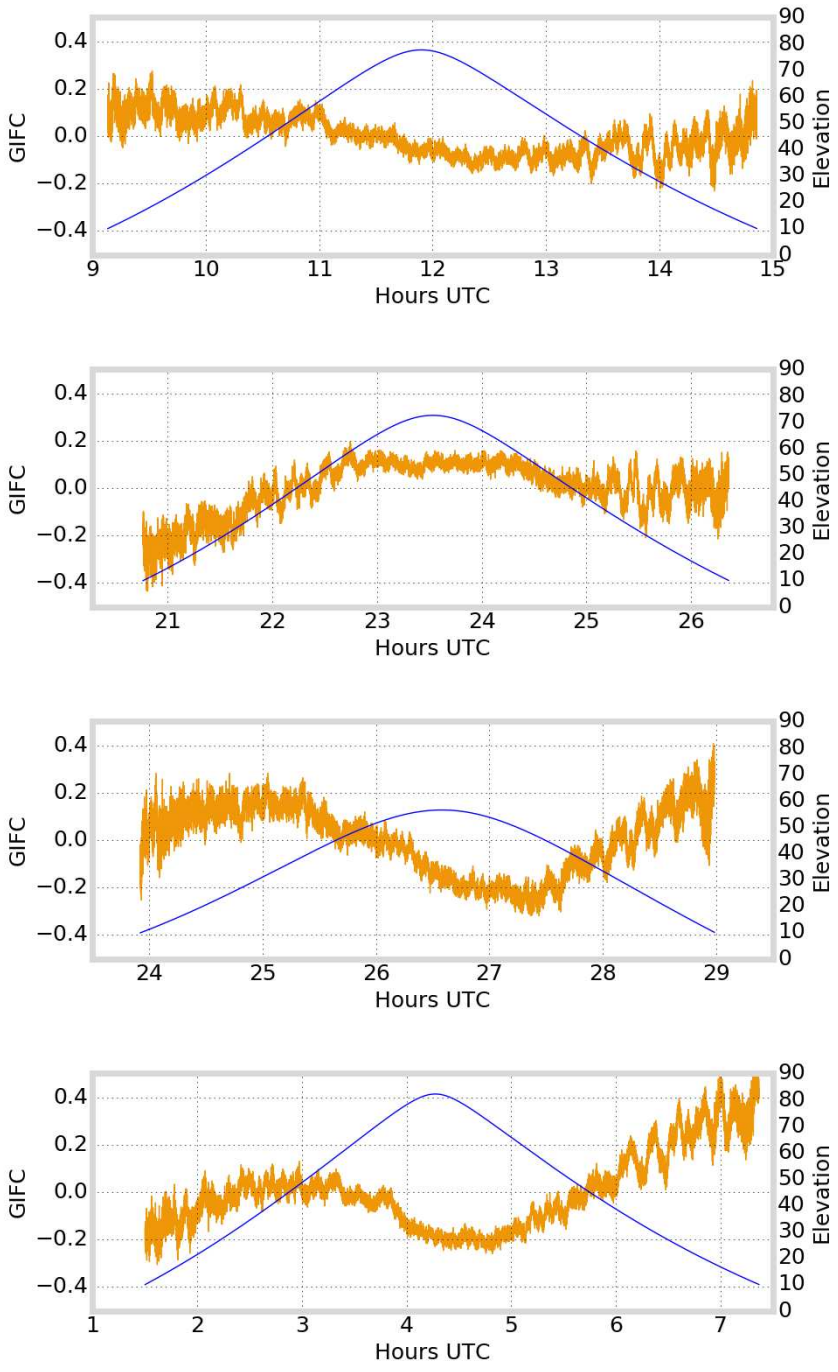

Figure 3.6: Shows nominal GIFC (orange line) of satellites G01, G24, G25, and G27 during quiet day for a receiver at Hok Tsui near Hong Kong. Satellite elevation is also shown (blue line).

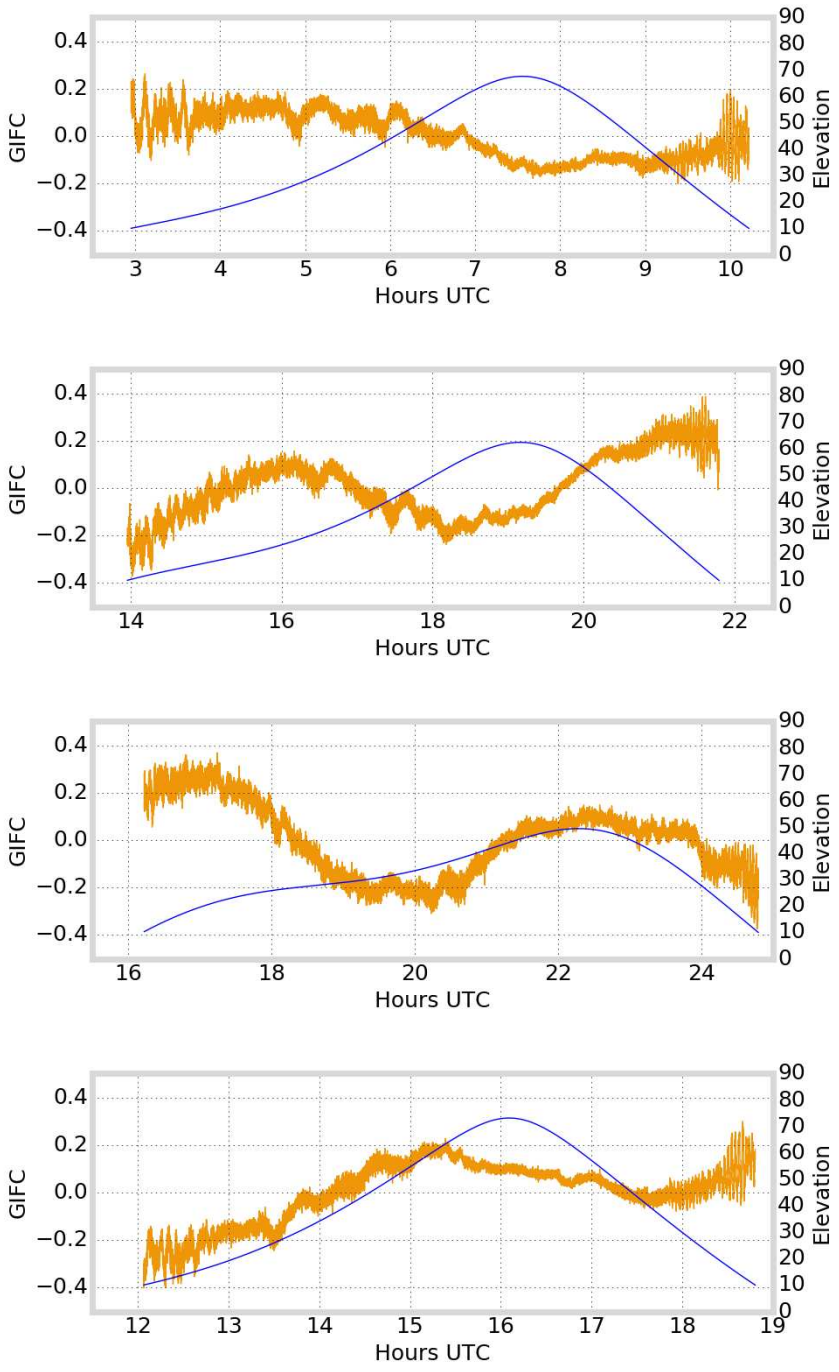

Figure 3.7: Shows nominal GIFC (orange line) of satellites G01, G24, G25, and G27 during quiet day for a receiver at Jicamarca, Peru. Satellite elevation is also shown (blue line).

period of weeks or months. Despite frequent data outages, the images appear to indicate an annual or quasi-annual pattern in the variation of these trends. Data from the receiver at Hok Tsui shows the clearest example of this pattern. It appears that the pattern may occur slightly earlier (around 7 days) from one year to the next.

3.3.3 GIFC Distribution

Figures 3.11, 3.12, and 3.13 show heatmaps of the GIFC signal amplitude over many passes. GIFC signals are leveled to zero-mean over the duration of the pass in order to emphasize the magnitude of unbiased residual errors. Multipath oscillations towards the ends of the pass are visible in these heatmaps. The GIFC deviations from zero vary for different satellites and receiver locations, however they all stay within roughly $\pm$ 0.5.

Table 3.1 shows certain percentile deviation values for the combination of all GIFC signals (for all satellites, receiver locations, and days) used in this study. It relates these percentile deviations to corresponding deviations of its component in each TEC estimation using scale factors from the third column of Table 2.3. Table 3.2 is similar to Table 3.1, except that it relates GIFC percentile deviations to corresponding overall deviations for each TEC estimation using scale factors from the fourth column of Table 2.3. This relation assumes independence and symmetric distributions of S_i as discussed in Section 2.7.

Under these assumptions, comparison of the two tables reveals that the unobservable error component still has a significant impact on $\mathrm{TEC_{L1,L2}}$, increasing the error residual deviations by a factor of around 1.5. A conservative bound would be that residual error deviations in $\mathrm{TEC_{L1,L2}}$ are usually less than 0.25 TECu. Meanwhile, $\mathrm{TEC_{L2,L5}}$ likely has error deviations surpassing 1.0 TECu. The GIFC error component in $\mathrm{TEC_{L1,L5}}$ is fairly small, at less than 0.07 TECu. Under the assumptions made for Table 3.2, its performance difference versus $\mathrm{TEC_{L1,L2,L5}}$ goes down to just over 0.01 TECu. Overall, we can say that the increase in frequency margin by introducing $L5$ signals has the biggest impact on improving

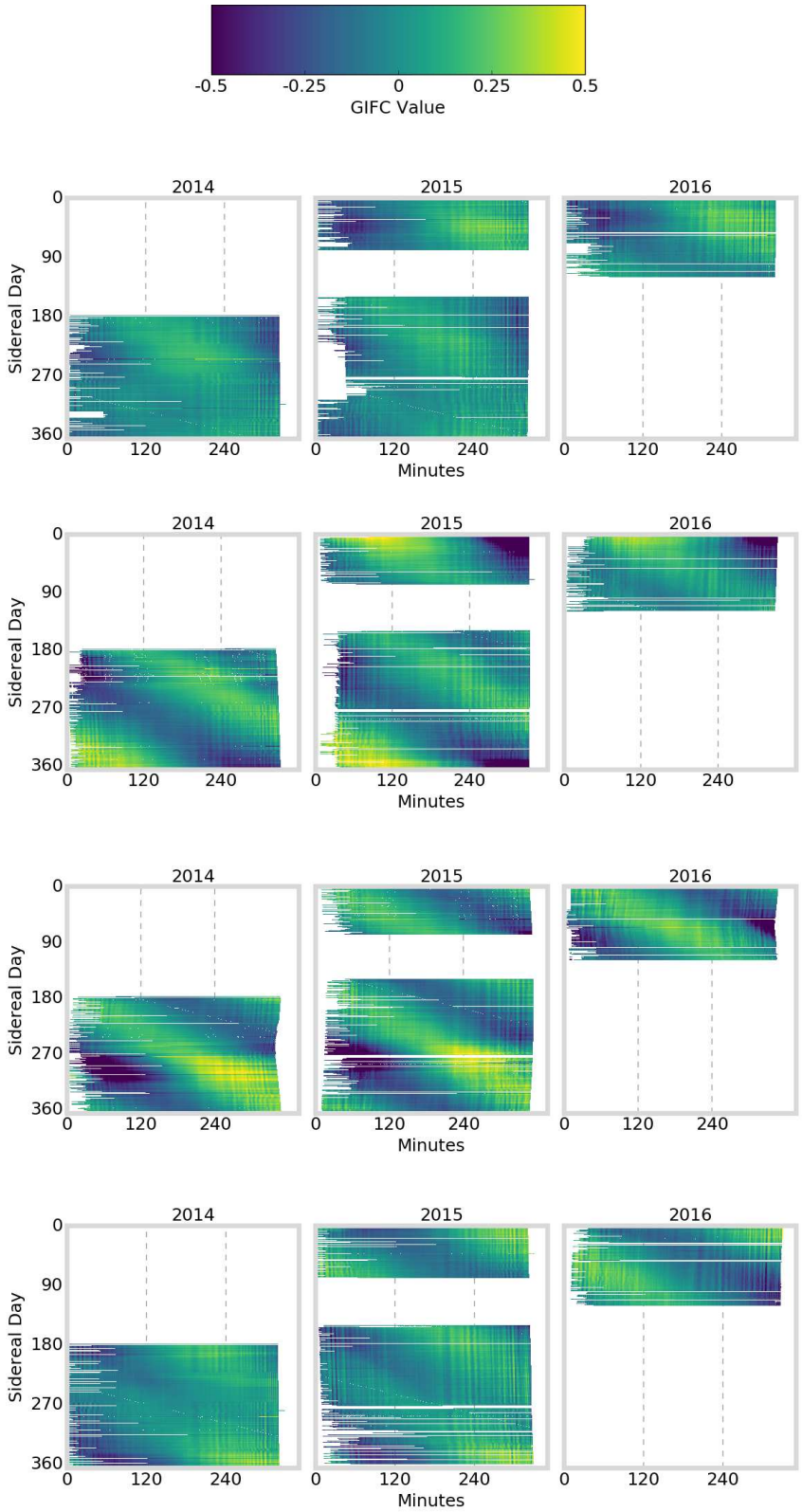

Figure 3.8: Shows how GIFC for satellites G01, G24, G25, and G27 changes over the course of 3 years for receiver in Poker Flat, Alaska.

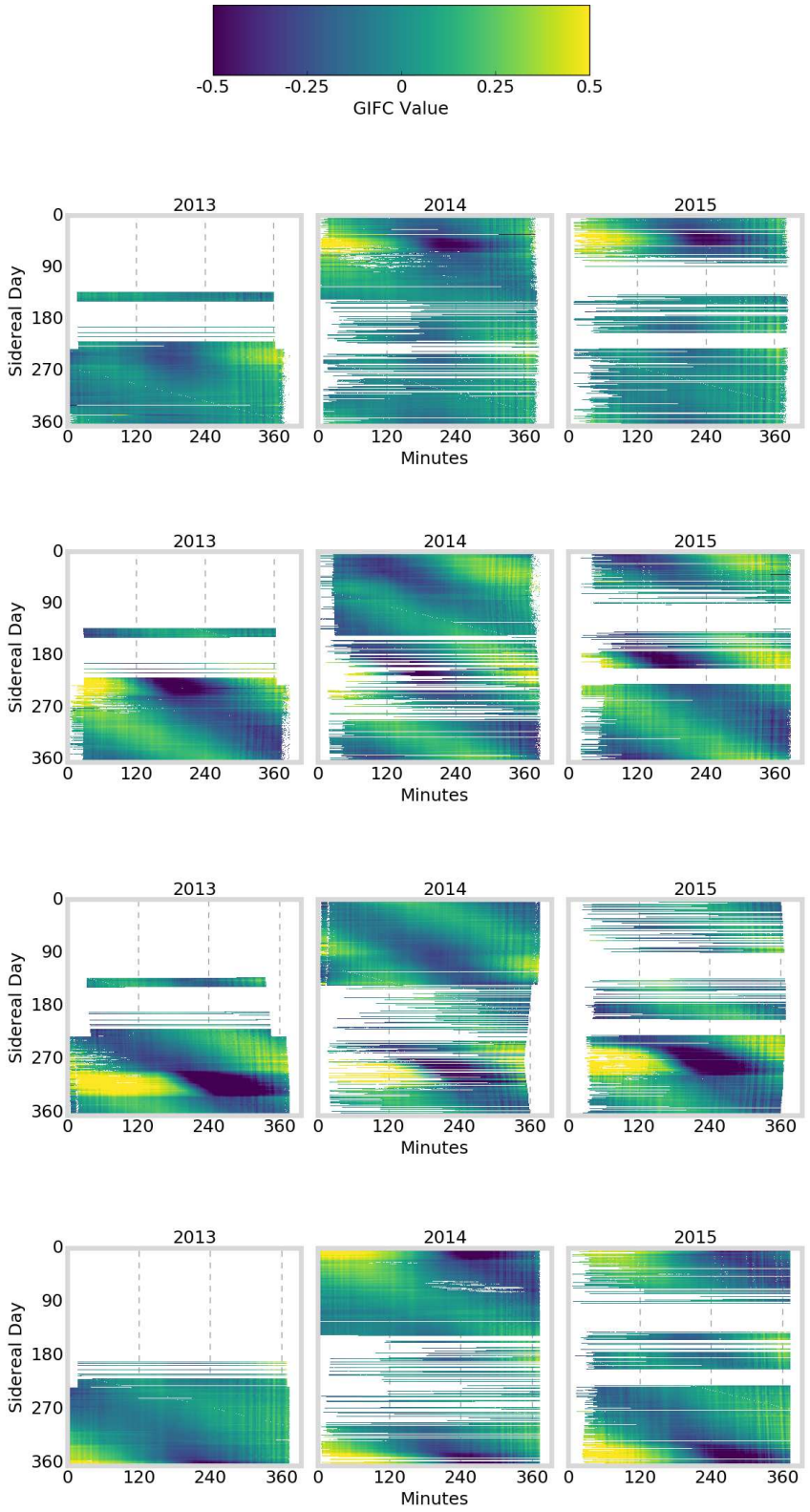

Figure 3.9: Shows how GIFC for satellites G01, G24, G25, and G27 changes over the course of 3 years for receiver in Hok Tsui, Hong Kong.

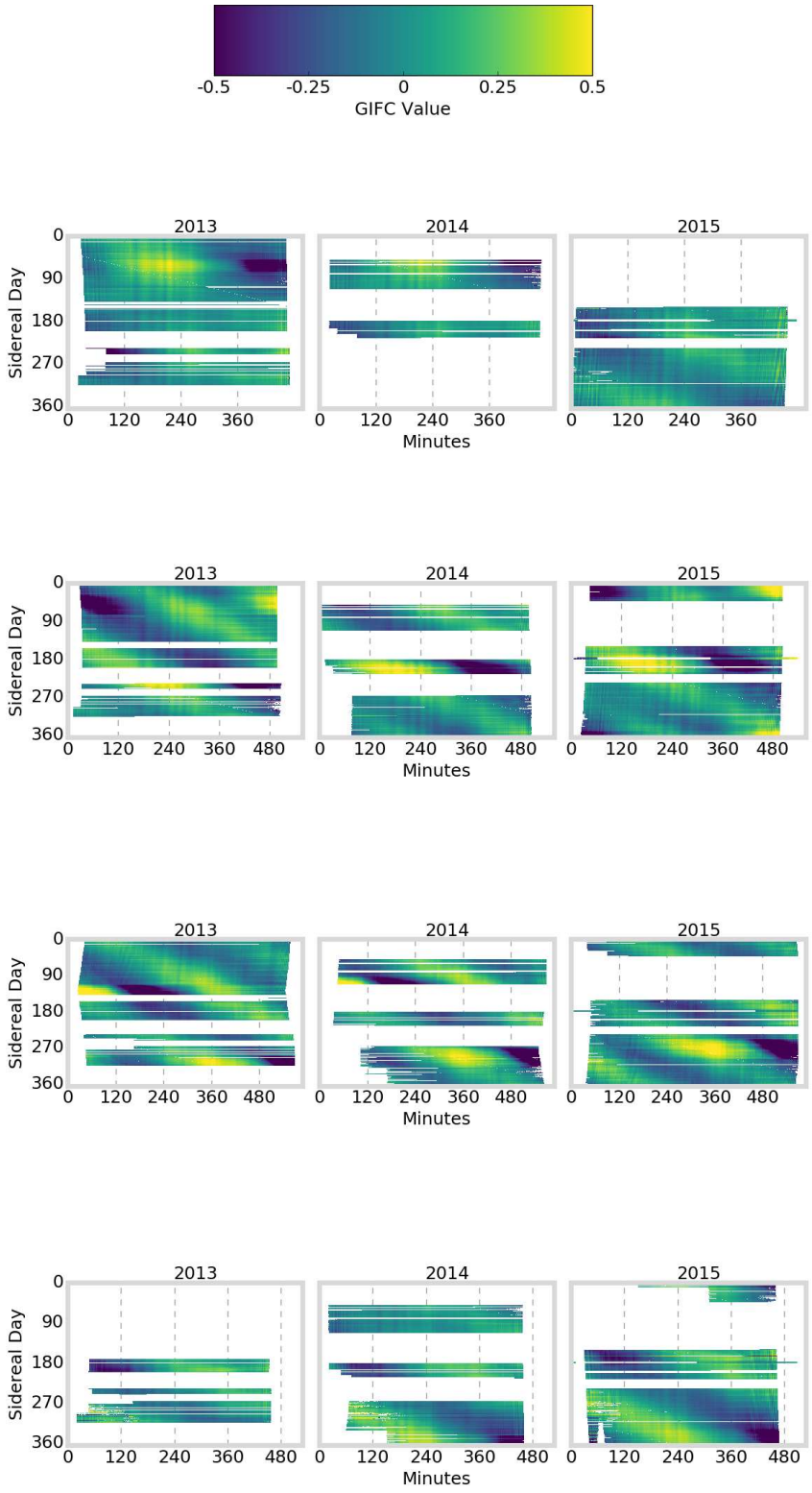

Figure 3.10: Shows how GIFC for satellites G01, G24, G25, and G27 changes over the course of 3 years for receiver in Jicamarca, Peru.

error suppression performance, though using all three frequencies does still improve error suppression a small amount.

Table 3.1: Shows GIFC deviation corresponding to chosen percentiles computed over the combined data (satellites G01, G24, G25, G27 at all three sites for all available days during 2013-2016). The columns to the right show how these deviations scale for each TEC estimation.

GIFC Deviation for Given Percentiles and Their Component Scaling to Error Deviations for TEC Estimates

Deviation Percentile	GIFC	$\text{TEC}_{\text{L1,L2,L5}}$	$\text{TEC}_{\text{L1,L5}}$	$\text{TEC}_{\text{L1,L2}}$	$\text{TEC}_{\text{L2,L5}}$
50	0.11	0	0.033	0.077	0.520
75	0.19	0	0.058	0.132	0.897
90	0.21	0	0.064	0.146	0.992

Table 3.2: Shows GIFC deviation similar to Table 3.1. The columns to the right show how these deviations scale for residuals in each TEC estimation according to the factor $\frac{||\mathbf{C}_{\text{TEC}}||}{||\mathbf{C}_{\text{GIFC}}||}$ and based on the assumptions/argument at the end of Section 2.7.

GIFC Deviation for Given Percentiles and Their Overall Scaling to Error Deviations for TEC Estimates

Deviation Percentile	GIFC	$\text{TEC}_{\text{L1,L2,L5}}$	$\text{TEC}_{\text{L1,L5}}$	$\text{TEC}_{\text{L1,L2}}$	$\text{TEC}_{\text{L2,L5}}$
50	0.11	0.091	0.097	0.119	0.528
75	0.19	0.158	0.168	0.206	0.911
90	0.21	0.175	0.186	0.228	1.007

3.3.4 TEC Results

For our last section of results, we present visual comparisons of actual TEC estimates using the triple-frequency GPS coefficients that we have discussed. We estimate TEC and related ambiguity and inter-frequency bias terms as discussed in Section 1.2.2 and in Appendix AA. Figures 3.14, 3.15, and 3.16 show a succession of TEC estimates, first showing all triple-frequency TEC estimates and then showing closeup examples from satellite G08, for a receiver in Poker Flat, Alaska. As we would expect, the L2/L5 TEC estimates show the most noise and deviation. Figure 3.15 shows the full pass for satellite G08, revealing the larger and slowly-changing discrepancy between L1/L5 and L1/L2 TEC estimates corresponding

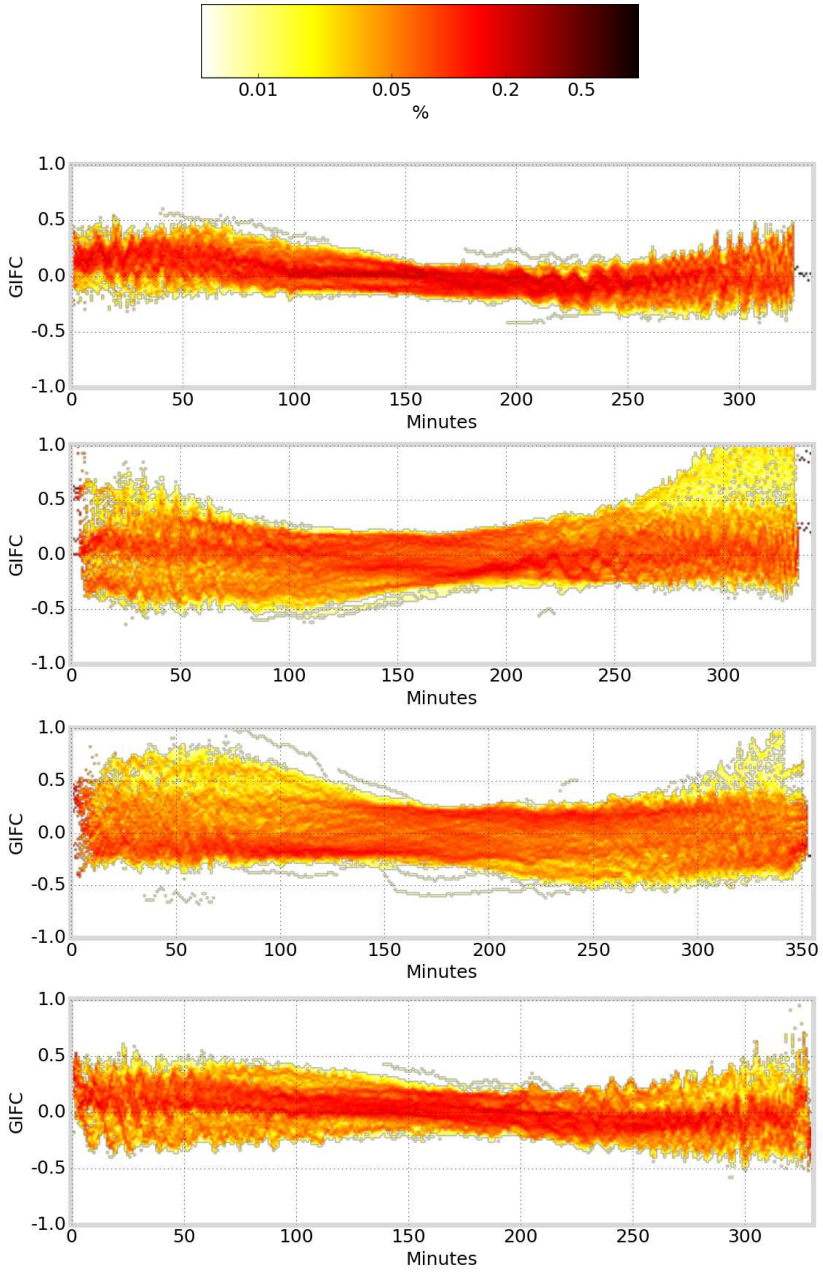

Figure 3.11: Shows heatmap of zero-mean GIFC values for satellites G01, G24, G25, and G27 and all available passes during 2013-1015 for receiver in Poker Flat, Alaska.

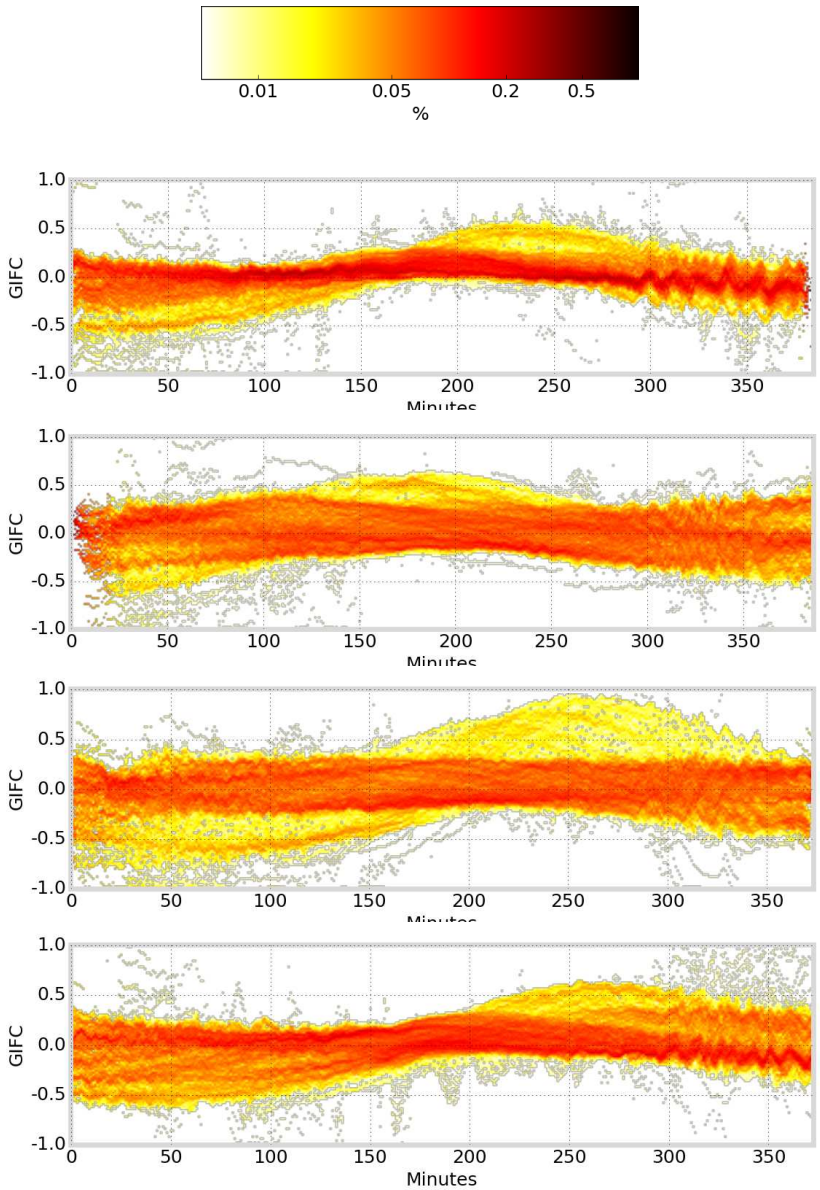

Figure 3.12: Shows heatmap of zero-mean GIFC values for satellites G01, G24, G25, and G27 and all available passes during 2013-1015 for receiver in Hok Tsui near Hong Kong.

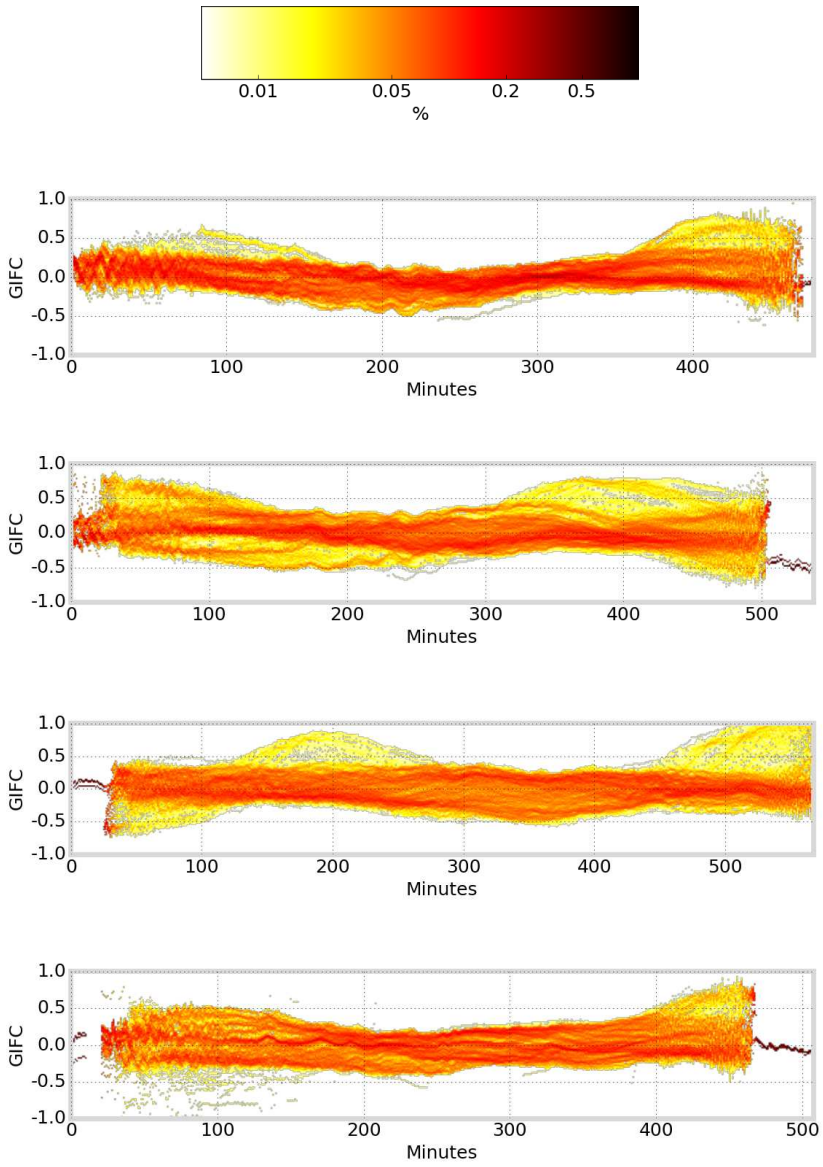

Figure 3.13: Shows heatmap of zero-mean GIFC values for satellites G01, G24, G25, and G27 and all available passes during 2013-1015 for receiver in Jicamarca, Peru.

to the low-frequency trend in the GIFC. We also see that the triple-frequency linear combination and least-squares TEC estimates lie between the dual-frequency L1/L2 and L1/L5 TEC estimates. The closeup example in Figure 3.16 shows that these estimates are almost identical, with the linear combination estimate showing a slightly stronger preference for the L1/L5 estimate compared to least-squares. Their similarity should be expected, as both are optimized geometry-free estimates of TEC using all three signals. Any discrepancies between the linear combination and least-squares estimate are likely due to the impact of the code-minus-carrier observations used in the least-squares estimate. Upon close examination of the L1/L5 and L1/L2 estimates, it appears that the L1/L2 estimate is slightly noisier, as should be expected based on its larger coefficient norm. Figure 3.16 also reveals the potential for triple-frequency estimates to reduce the effects of multipath, as certain sections show that the triple-frequency estimates oscillate noticeably less than the dual-frequency estimates.

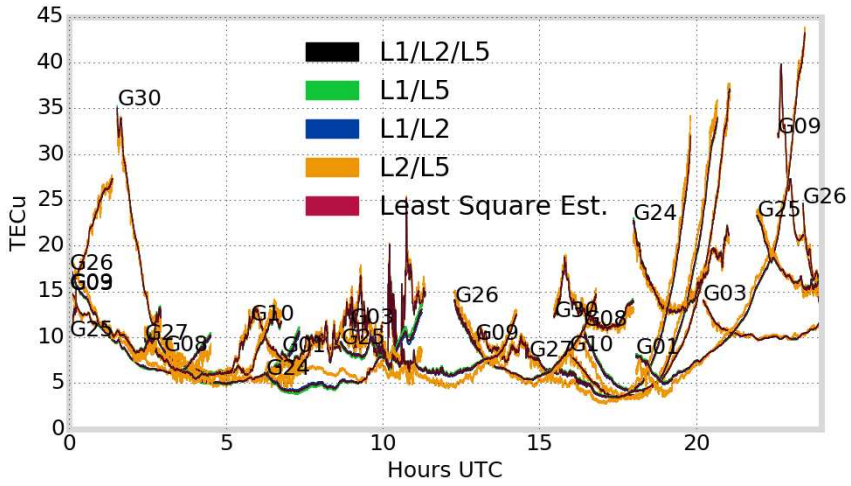

Figure 3.14: Shows comparison of TEC estimates for all triple-frequency satellites for receiver in Poker Flat, Alaska on 2016-01-02. The L2/L5 estimates are by far the noisiest.

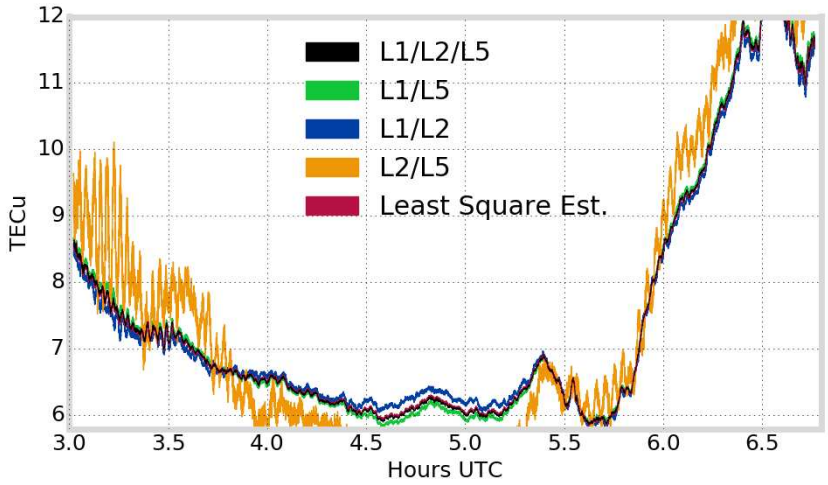

Figure 3.15: Shows comparison of TEC estimates for satellite G08 as a closeup example of results shown in Figure 3.14. The triple-frequency L1/L2/L5 and least squares estimates are essentially identical, and they lie between the L1/L2 and L1/L5 TEC estimates. The low-frequency discrepancy between L1/L5 and L1/L2 estimates can especially be seen between hours 4.5 to 5.5.

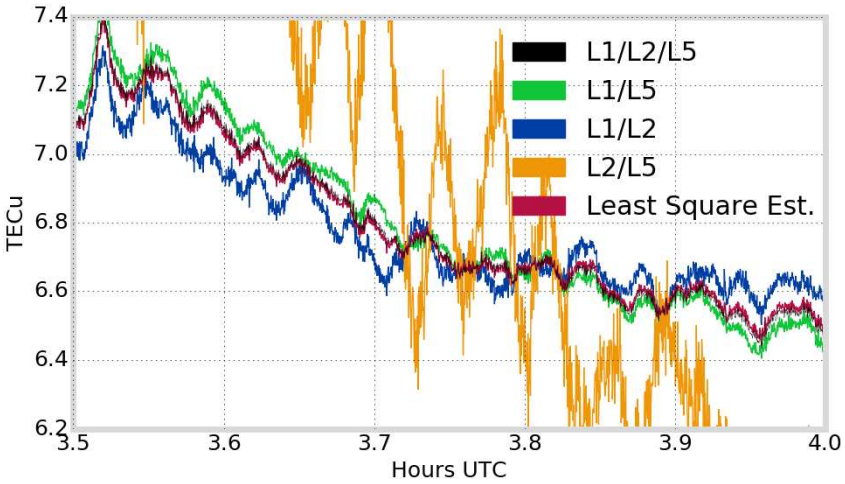

Figure 3.16: Shows closeup comparison of TEC estimates as shown in Figure 3.15. Multi-path fluctuations can be seen in both dual-frequency and triple-frequency estimates, however, there are sections (such as between hours 3.6 to 3.7) that the triple-frequency TEC estimates appear to have less fluctuation than either L1/L2 or L1/L5 estimates. The triple-frequency linear combination and least-squares estimates are nearly identical, with the linear combination estimate showing a slight preference for the L1/L5 over the L1/L2 TEC estimate when compared to the least-squares estimate.

CHAPTER 4: DISCUSSION AND CONCLUSION

4.1 Summary of Work

In this work, we first introduced a simple model for GNSS phase pseudorange observables. We then derived linear model estimators that combine the GNSS phase pseudoranges. We limited our focus to the precision (rather than overall accuracy) of these estimates by not considering bias terms from our model. The choice of estimator coefficients was motivated by the assumption that $|G| \gg |I_i| \gg |S_i|$. We showed optimal triple-frequency combinations for geometry-free TEC estimators, ionosphere-free geometry estimators, and the geometry-ionosphere-free estimator of systematic errors. We discussed how, under certain strong assumptions, the GIFC can be related to the error residuals in linear TEC estimates.

Our analysis proceeded by computing the GIFC signal for multiple satellites across three receiver locations over the span of 3.5 years. The results showed that 1) a large, slowly-varying trend dominates the GIFC signal, followed by multipath and then other systematic errors, 2) this trend shows quasi-annual pattern, 3) that moderate to high scintillation activity corresponds to an increase in GIFC noise levels, and 4) that the zero-mean GIFC deviations tend to stay well below 0.5, with 50% deviation at 0.11 and 90% deviation at 0.21 across all datasets. Relating the GIFC deviations to triple-frequency GPS TEC estimates suggests that dual-frequency TEC estimates using GPS L1/L2 signals have residual errors whose distribution in magnitude is similar to that of the GIFC. A conservative bound based on the assumptions at the end of Section 2.7 suggests that residual errors in $\mathrm{TEC}_{\mathrm{L1,L2}}$ are generally less than 0.25 TECu.

We also compared dual-frequency and triple-frequency TEC estimates for a one-day example. The results for these estimates corresponded to our expectations based on our derivations and the coefficient magnitudes. Namely, the L2/L5 combination is noisiest, followed by L1/L2 and then L1/L5. The triple-frequency linear combination is shown to lie between the L1/L5 and L1/L2 TEC estimates and appears to have the potential to reduce the effect

of multipath in certain scenarios. We also found the triple-frequency linear combination and least-squares estimates to be nearly identical, which should be expected based on the similarities in their derivations (i.e. geometry-free, identical noise for all three signals). We note here that the triple-frequency linear combination offers a simpler estimation procedure than least-squares. When only relative TEC is needed, the linear combination triple-frequency estimate will be useful.

4.2 Implications

There are several important implications of the results we presented. As for the quasi-annual variations in the large-scale trend of GIFC, it is plausible that these large-scale features in the GIFC signals may correspond to satellite antenna phase effects. The fact that the feature occurs over the course of the entire satellite pass and that it repeats from day-to-day indicate some effect involving the satellite-receiver geometry. Additionally, the yearly pattern they seem to follow corresponds to the timescale for changes in the receiver-satellite-Sun geometry that determines the satellite attitude. Though the mean phase center of GPS L1/L2 has been investigated for Block IIF satellites, the mean phase centers for combinations including L5 have yet to be investigated [29].

If the large-scale trend can be modeled and removed, then the GIFC becomes useful for studying the remaining systematic effects. In particular, it may be a useful metric for analyzing performance of multipath mitigation and estimation of higher-order ionosphere terms. This type of performance analysis may prove convenient in the context of precise point positioning where addressing these effects is critical. More can and should be said about the nature of the GIFC and its underlying components. Time-frequency and independent component analysis may be applicable.

The GIFC residual error contribution to $\mathrm{TEC}_{\mathrm{L1,L2}}$ in Table 3.1 suggests that, in general, residual errors impacting $\mathrm{TEC}_{\mathrm{L1,L2}}$ are larger than 0.1 TECu. This would mean that error residuals impact studies such as [30], which studies plasma bubbles with rate-of-TEC indexes

and cites observations of TEC fluctuations of over 0.05 TECu /minute to be significant (i.e. not due to residual errors). However, because most of the GIFC deviation we measured is due to large-scale trends, these figures seem like a reasonable precision.

4.3 Future Work

There are several paths to continue the work laid out in this thesis. Foremost among these is investigation into actual causes for the systematic errors present in the GIFC. Investigating satellite antenna phase center variations is a good starting point. Signal components corresponding to higher-order ionosphere terms and phase-windup effects, which vary slowly over the course of the pass, are dominated by the large-scale trend. If the large-scale trend can be modeled and removed, then adding higher-order ionosphere effects to the model may be a straightforward next step. Additionally, we plan to perform simulations in order to investigate the unobservable component of TEC estimation residual error. In particular, we hope to isolate and further characterize the specific error impact of ionosphere activity. Finally, the assumptions used to derive TEC estimation precision should be explored further. In particular, it would be helpful to have better statistics on the noise characteristics of each signal, as well as a better understanding of the relative size of impact of different systematic errors.

REFERENCES

[1] M. C. Kelley, Ed., *The Earth's Ionosphere, Plasma Physics and Electrodynamics*. Elsevier, 2009, vol. 96.

[2] G. C. Corazza, "Marconi's history [radiocommunication]," *Proceedings of the IEEE*, vol. 86, no. 7, pp. 1307–1311, 1998.

[3] E. J. Petrie, M. Hern´andez-Pajares, P. Spalla, P. Moore, and M. A. King, "A review of higher order ionospheric refraction effects on dual frequency GPS," *Surveys in geophysics*, vol. 32, no. 3, pp. 197–253, 2011.

[4] CDAAC, "CDAAC radio occultation Level2 ionPrf dataset," 2017. [Online]. Available: ftp://cdaac-ftp.cosmic.ucar.edu/

[5] IGS, "IGS IONEX global TEC maps," 2017. [Online]. Available: ftp://ftp.igs.org/

[6] J. Lei, L. Liu, W. Wan, and S.-R. Zhang, "Variations of electron density based on long-term incoherent scatter radar and ionosonde measurements over Millstone Hill," *Radio science*, vol. 40, no. 2, 2005.

[7] T. Tsugawa, Y. Otsuka, A. Coster, and A. Saito, "Medium-scale traveling ionospheric disturbances detected with dense and wide TEC maps over North America," *Geophysical Research Letters*, vol. 34, no. 22, 2007.

[8] A. Komjathy, Y.-M. Yang, X. Meng, O. Verkhoglyadova, A. J. Mannucci, and R. B. Langley, "Review and perspectives: Understanding natural-hazards-generated ionospheric perturbations using GPS measurements and coupled modeling," *Radio Science*, vol. 51, no. 7, pp. 951–961, 2016.

[9] P. Misra and P. Enge, "Global positioning system: Signals, measurements and performance second edition," *Massachusetts: Ganga-Jamuna Press*, 2006.

[10] L. Ciraolo, F. Azpilicueta, C. Brunini, A. Meza, and S. Radicella, "Calibration errors on experimental slant total electron content (TEC) determined with GPS," *Journal of Geodesy*, vol. 81, no. 2, pp. 111–120, 2007.

[11] D. Kim and R. B. Langley, "GPS ambiguity resolution and validation: methodologies, trends and issues," in *Proceedings of the 7th GNSS Workshop–International Symposium on GPS/GNSS, Seoul, Korea*, vol. 30, no. 2.12, 2000.

[12] W. Chen, C. Hu, S. Gao, Y. Chen, X. Ding, and C. K. Simon, "Absolute ionospheric delay estimation based on GPS PPP and GPS active network," in *2004 International Symposium on GNSS/GPS, Sydney, Australia*, 2004.

[13] A. Hansen, "Real-time ionospheric tomography using terrestrial GPS sensors," in *PROCEEDINGS OF ION GPS*, vol. 11. INSTITUTE OF NAVIGATION, 1998, pp. 717–728.

[14] H. W. Bourne, "An algorithm for accurate ionospheric total electron content and receiver bias estimation using GPS measurements," Master's thesis, Colorado State University. Libraries, 2016.

[15] O. Julien, M. E. Cannon, P. Alves, and G. Lachapelle, "Triple frequency ambiguity resolution using GPS/Galileo," *Eur J Navig*, vol. 2, no. 2, pp. 51–56, 2004.

[16] M. Cocard, S. Bourgon, O. Kamali, and P. Collins, "A systematic investigation of optimal carrier-phase combinations for modernized triple-frequency GPS," *Journal of Geodesy*, vol. 82, no. 9, pp. 555–564, 2008.

[17] B. Li, Y. Feng, and Y. Shen, "Three carrier ambiguity resolution: distance-independent performance demonstrated using semi-generated triple frequency GPS signals," *GPS solutions*, vol. 14, no. 2, pp. 177–184, 2010.

[18] L. Pan, X. Zhang, X. Li, J. Liu, and X. Li, "Characteristics of inter-frequency clock bias for Block IIF satellites and its effect on triple-frequency GPS precise point positioning," *GPS Solutions*, pp. 1–12.

[19] J. Spits and R. Warnant, "Total electron content monitoring using triple frequency gnss data: A three-step approach," *Journal of Atmospheric and Solar-Terrestrial Physics*, vol. 70, no. 15, pp. 1885–1893, 2008.

[20] J. Ray and M. Cannon, "Characterization of GPS carrier phase multipath," in *Proceedings of ION National Technical Meeting*, 1999, pp. 243–252.

[21] M. M. Hoque and N. Jakowski, "Estimate of higher order ionospheric errors in GNSS positioning," *Radio Science*, vol. 43, no. 5, 2008.

[22] IGS, "IGS ANTEX file," 2014. [Online]. Available: https://igscb.jpl.nasa.gov/igscb/station/general/igs14.atx

[23] F. Dillsner, "GPS IIF-1 satellite antenna phase center and attitude modeling," *Inside GNSS*, pp. 59–63, September 2010.

[24] P. Heroux, J. Kouba, P. Collins, and F. Lahaye, "GPS carrier-phase point positioning with precise orbit products," in *Proceedings of the KIS*, 2001, pp. 5–8.

[25] D. Odijk, "Ionosphere-free phase combinations for modernized GPS," *Journal of surveying engineering*, vol. 129, no. 4, pp. 165–173, 2003.

[26] J. Spits and R. Warnant, "Total electron content monitoring using triple frequency GNSS: Results with Giove-A/-B data," *Advances in Space Research*, vol. 47, no. 2, pp. 296–303, 2011.

[27] M. Hernández-Pajares, J. Juan, and J. Sanz, "Medium-scale traveling ionospheric disturbances affecting GPS measurements: Spatial and temporal analysis," *Journal of Geophysical Research: Space Physics*, vol. 111, no. A7, 2006.

[28] Y. Jiao, Y. Morton, and S. Taylor, "Comparative studies of high-latitude and equatorial ionospheric scintillation characteristics of GPS signals," in *Position, Location and Navigation Symposium-PLANS 2014, 2014 IEEE/ION*. IEEE, 2014, pp. 37–42.

[29] R. Schmid, R. Dach, X. Collilieux, A. Jäggi, M. Schmitz, and F. Dilssner, "Absolute IGS antenna phase center model igs08.atx: status and potential improvements," *Journal of Geodesy*, vol. 90, no. 4, pp. 343–364, 2016.

[30] M. Nishioka, A. Saito, and T. Tsugawa, "Occurrence characteristics of plasma bubble derived from global ground-based GPS receiver networks," *Journal of Geophysical Research: Space Physics*, vol. 113, no. A5, 2008.

APPENDIX

AA Multi-Frequency Least-Squares TEC Estimation

This documents our implementation of TEC estimation using triple-frequency measurements, which is similar to that in [19]. However, there are some differences, so here we document our exact method of implementation.

In order to estimate absolute TEC, carrier ambiguity and inter-frequency hardware bias terms must be estimated. For this we use a code-carrier leveling method as part of the linear system used to estimate TEC. To discuss this method, we first introduce two new and separate equations for code and carrier (P and Φ) pseudorange observations:

$$P_i = G + I_{P_i} + H_{s_i} + H_{r_i} + S_{P_i} + \epsilon_{P_i} \tag{A-1}$$

$$\Phi_i = G + I_{\Phi_i} + H_{s_i} + H_{r_i} + \lambda_i N_i + S_{\Phi_i} + \epsilon_{\Phi_i} \tag{A-2}$$

where i denotes terms corresponding to a particular signal at frequency f_i, G contains the sum of all non-dispersive terms as developed in Section 2.1, I_{P_i} and I_{Φ_i} are the ionosphere delays corresponding to code and carrier measurements respectively, H_{s_i} and H_{r_i} are hardware delays corresponding to the satellite and receiver respectively, and the terms S_{P_i}, S_{Φ_i}, ϵ_{P_i} and ϵ_{Φ_i} are the systematic and stochastic error terms corresponding to code and carrier measurements respectively. It is worth clarifying that in general, hardware delays can be different for code and carrier measurements, creating a code-carrier bias. For the Septentrio receiver used in this study, code-carrier bias is effectively zero by design, and so hardware delays are assumed equal on code and carrier in our model.

Here, unlike in the main text, we distinguish the ionosphere effect on code and carrier. Their first-order effects, which are sufficient for our analysis and are also assumed in [19] can

be modeled as:

$$I_{P_i} = \frac{\kappa_u}{f_i^2}\text{TECu} \tag{A-3}$$

$$I_{\Phi_i} = -\frac{\kappa_u}{f_i^2}\text{TECu} \tag{A-4}$$

That is, the first-order ionosphere effect on code and carrier measurements are equal in magnitude and opposite in sign.

Another difference from in the main text is that we introduce hardware delays specific to satellite and receiver. Estimation of satellite hardware biases generally requires a network of ground receivers. Here, we apply satellite hardware bias estimated by IGS in their IONEX files [5]. This allows us to remove the terms H_{s_i} from equations A-3 and A-4.

Given triple-frequency observations, we form two geometry-free measurements called the carrier-difference and code-minus-carrier observables. By applying the previously estimated satellite hardware biases and substituting the ionosphere effect expressions in equations A-3 and A-4 we obtain:

$$\Phi_i - \Phi_j = \Delta\Phi_{i,j} = -\kappa\left(\frac{1}{f_i^2} - \frac{1}{f_j^2}\right)\text{TECu} + \Delta H_{i,j} + \langle\text{error terms}\rangle \tag{A-5}$$

for the carrier-difference expression and:

$$P_i - \Phi_i = \text{CMC}_i = 2\frac{\kappa_u}{f_i^2}\text{TECu} - \lambda_i N_i + \langle\text{error terms}\rangle \tag{A-6}$$

for the code-minus-carrier expression. Here, $\Delta H_{i,j} = H_{r_i} - H_{r_j}$ is the receiver inter-frequency hardware bias between signals i and j. Note that the code-minus-carrier expression no longer has the inter-frequency hardware bias term. However, because it contains code pseudorange measurements, its noise terms are much larger than those in the carrier-difference.

A linear model for estimating TEC and related inter-frequency and carrier ambiguity biases can be formed using these carrier-difference and code-minus-carrier expressions for triple-frequency measurements. The parameters to be estimated are TECu, $\lambda_1 N_1$, $\lambda_2 N_2$,

$\lambda_3 N_3$, $\Delta H_{1,2}$, and $\Delta H_{1,3}$. The portion of the system corresponding to contiguous (i.e. no loss-of-lock or cycle slips) observations from a particular satellite can be expressed as:

$$\begin{bmatrix} \Delta\Phi_{1,2_t} \\ \Delta\Phi_{1,3_t} \\ \Delta\Phi_{1,2_{t+1}} \\ \vdots \\ W_t \mathrm{CMC}_{1_t} \\ W_t \mathrm{CMC}_{2_t} \\ W_t \mathrm{CMC}_{3_t} \\ W_{t+1} \mathrm{CMC}_{1_{t+1}} \\ \vdots \end{bmatrix} = \begin{bmatrix} -\frac{\kappa_u}{\alpha_{1,2}} & 0 & \cdots & 1 & -1 & 0 & 1 & 0 \\ -\frac{\kappa_u}{\alpha_{1,3}} & 0 & \cdots & 1 & 0 & -1 & 0 & 1 \\ 0 & -\frac{\kappa_u}{\alpha_{1,2}} & \cdots & 1 & -1 & 0 & 1 & 0 \\ \vdots & & & & & & & \vdots \\ 2W_t \frac{\kappa_u}{f_1^2} & 0 & \cdots & -W_t & 0 & 0 & 0 & 0 \\ 2W_t \frac{\kappa_u}{f_2^2} & 0 & \cdots & 0 & -W_t & 0 & 0 & 0 \\ 2W_t \frac{\kappa_u}{f_3^2} & 0 & \cdots & 0 & 0 & -W_t & 0 & 0 \\ 0 & 2W_{t+1} \frac{\kappa_u}{f_1^2} & \cdots & -W_{t+1} & 0 & 0 & 0 & 0 \end{bmatrix} \begin{bmatrix} \mathrm{TECu}_t \\ \mathrm{TECu}_{t+1} \\ \vdots \\ \lambda_1 N_1 \\ \lambda_2 N_2 \\ \lambda_3 N_3 \\ \Delta H_{1,2} \\ \Delta H_{1,3} \end{bmatrix} \tag{A-7}$$

where $\alpha_{i,j} = \left(\frac{1}{f_i^2} - \frac{1}{f_j^2}\right)^{-1}$ and where W_t is a weight used to reduce the impact of code noise on the system's solution. The inclusion of the CMC terms into the full system model is the main difference between our implementation and the algorithm provided in [19] and [26], where carrier ambiguities are estimated separately. The weight W_t could change depending on other parameters, such as satellite elevation or presence of multipath, or it can be chosen to be constant. We choose to set $W_t = 0.001$ in order to bring the noise effects of the code observations below the level of carrier phase noise effects.

This system is repeated for each contiguous set of observations from each satellite, with a new set of ambiguity parameters $\lambda_i N_i$ being estimated for each segment and the receiver hardware biases $\Delta H_{1,2}$ and $\Delta H_{1,3}$ being shared across all satellites and data segments. A sparse iterative linear-least-squares solver is then used to find parameters TECu_t, $\lambda_i N_i$ and $\Delta H_{i,j}$. We refer to this TECu signal as the triple-frequency least-squares TEC estimate. The estimates of $\lambda_i N_i$ and $\Delta H_{i,j}$ can be used to correct dual-frequency TEC estimates for any signal pair.

After solving the system above, $\Delta H_{1,2}$ and $\Delta H_{1,3}$ will have correct offsets relative to one another, but will still be off by some constant. That is, $\Delta H_{1,2}$ and $\Delta H_{1,3}$ are relative inter-frequency hardware biases that do not reflect the overall inter-frequency hardware bias. In turn, all TEC estimates will also be offset by some constant. To estimate the overall inter-frequency hardware bias, we apply the TEC gradient mapping method as discussed in [14]. Our implementations are identical, and so the method will not be described here. The algorithm provides an absolute estimate of $\Delta H_{1,2}$, which we use to correct the inter-frequency biases and overall TEC estimated using triple-frequency signals.

AB GIFC Jump Correction

Here we describe in more detail our implementation of a jump-correction algorithm for the GIFC signal. The algorithm can be divided into three steps: finding no-jump segments, estimating jump amplitudes, and applying jump corrections. We should note that this algorithm differs from traditional cycle slip estimation and correction in that individual jump times are not detected.

We begin by taking the epoch-to-epoch difference of the GIFC signal. We consider all contiguous segments for which the magnitude of this difference does not exceed 0.2 for the GIFC units given in Equation 2.23. We associate one jump value per segment. We simultaneously estimate jump values and a 3rd-order polynomial fit to the entire GIFC signal for a given pass using the following system, which is a modified Vandermonde matrix:

$$\text{GIFC} = \begin{bmatrix} 1 & t_0 & t_0^2 & 0 & 0 & \cdots \\ 1 & t_1 & t_1^2 & 0 & 0 & \cdots \\ \vdots & \vdots & \vdots & \vdots & \vdots & \cdots \\ 1 & t_{k-1} & t_{J_1-1}^2 & 0 & 0 & \cdots \\ 1 & t_k & t_{J_1}^2 & 1 & 0 & \cdots \\ \vdots & \vdots & \vdots & \vdots & \vdots & \cdots \\ 1 & t_L & t_L^2 & 1 & 1 & \cdots \end{bmatrix} \begin{bmatrix} p_0 \\ p_1 \\ p_2 \\ J_1 \\ \vdots \end{bmatrix} \tag{A-8}$$

where p_i are the polynomial coefficients and J_i are the jump amplitudes. The system in Equation A-8 is solved for the least-squares estimate of $[p_0, p_1, p_2, J_1, \cdots]^T$. The jump estimates J_i are then used to correct the individual no-jump segments of the GIFC. GIFC epochs that did not satisfy the no-jump threshold test described above are removed from the analysis by setting their values to NaN.